

Abstract

This study investigates the spontaneous self-aggregation of convection in non-rotating Radiative-Convective Equilibrium (RCE) simulations performed by the CNRM-CM6-1 General Circulation Model within the framework of the RCE Model Intercomparison Project (RCEMIP). In this model, the level of convection self-aggregation at equilibrium, as quantified by metrics based on moisture or moist static energy, strongly increases with sea surface temperature (SST). As it gets warmer, the troposphere gets drier, high cloud cover diminishes in dry regions, the top of high cloud rises and their thickness increases in moist regions, and low cloud cover increases. At high SSTs, the large-scale circulation exhibits a shallow component, stronger than its deep counterpart. The transition towards self-aggregation has a similar first 20-day phase for all SSTs within the 295–305-K range. It primarily involves radiative positive feedback processes. Then, for SSTs above approximately 300 K, a new, slower, transition towards higher levels of self-aggregation occurs. It is concomitant with a shift from a top-heavy to a more bottom-heavy large-scale circulation, a strengthening of the shallow circulation and a reduced mobility of convective aggregates. This second transition is mostly driven by the dry regions, still involves longwave radiative positive feedbacks, but also advective positive feedbacks in the driest regions. It is argued that boundary-layer radiative cooling difference between moist and dry regions, which is stronger at high SSTs, is instrumental in this second phase of self-aggregation. The sensitivity of deep convection to environmental dry air also likely acts as a positive feedback on the system.

Plain Language Summary

In idealized configurations of the Earth, convective clouds can spontaneously organize into large clusters: this is convective self-aggregation. We investigate the sensitivity of this process to surface temperature in the atmospheric component of the state-of-the-art global climate model CNRM-CM6-1. For surface temperatures spanning a typical range of tropical conditions (295–305 K), the model exhibits an aggregated state when equilibrium is reached. As the surface gets warmer, convection is more aggregated, the troposphere gets drier, high clouds get less frequent in dry regions and low cloud cover increases. When starting from homogeneous conditions, an initial rapid phase of self-aggregation occurs in all experimented SST. Radiative processes are instrumental in leading to self-aggregation. For warm surface temperature above approximately 300 K, a second, slower,

46 transition occurs and leads to higher levels of self-aggregation. It is associated with an
47 adjustment of the large-scale circulation, in which shallow circulations in the lower tro-
48 phosphere (surface-700 hPa) and between dry and moist regions strengthens. The radia-
49 tive loss of energy within the boundary layer, and its unbalanced state between dry and
50 moist regions after the initial transition is argued to be the main process at play.

51 **1 Introduction**

52 Tropical deep convection organizes across a wide range of scales, driven by a va-
53 riety of physical processes. It can be forced by equatorial waves (Kiladis et al., 2009),
54 topography or surface temperature gradients, either above ocean (Shamekh et al., 2020a),
55 land (Becker & Stevens, 2014; Hohenegger & Stevens, 2018) or at the boundaries between
56 both types of surface (Coppin & Bellon, 2019a, 2019b). At mesoscale, convection is able
57 to generate its own sources of organization as is the case for Mesoscale Convective Sys-
58 tems (Houze, 2004) or squall lines (Rotunno et al., 1988). At larger scales, large convec-
59 tive envelopes such as the Madden-Julian Oscillation (Madden & Julian, 1994) or var-
60 ious forms of organization along the equator are also able to modify the average zonal
61 or meridional circulations (Bellenger et al., 2009).

62 One type of organization that arises in idealized numerical simulations, such as un-
63 der the Radiative-Convective Equilibrium (RCE) hypothesis, is self-aggregation (e.g., Wing,
64 2019). This spontaneous organization of deep convection has been studied in a wide range
65 of models, from small-domain large-eddy or cloud-permitting simulations (Bretherton
66 et al., 2005; Muller & Held, 2012; Tompkins & Semie, 2017) to global, Earth-scale sim-
67 ulations with general circulation models (GCM – Popke et al., 2013; Coppin & Bony,
68 2015; Becker et al., 2017), and under a wide range of surface boundary conditions: from
69 fixed and uniform surface temperature (Khairoutdinov & Emanuel, 2013; Wing & Emanuel,
70 2014; Cronin & Wing, 2017) to an interactive surface, based on an ocean mixed-layer
71 model (Coppin & Bony, 2017, 2018; Shamekh et al., 2020b). These models share the same
72 drying of the free troposphere as convection aggregates and the subsequent increase in
73 outgoing longwave radiation to space (Bretherton et al., 2005; Holloway et al., 2017; Wing
74 et al., 2017). This atmospheric response to convective aggregation is also consistent with
75 observations (Tobin et al., 2012, 2013; Stein et al., 2017). In contrast, models do not agree
76 on the sensitivity of aggregation to sea surface temperature (SST) nor on the details of
77 the various mechanisms controlling the initiation, maintenance or inhibition of convec-

78 tive aggregation. For example, in contrast to Cloud Permitting Models (CPM), aggregation
79 almost always increases with SST in GCMs (Becker & Wing, 2020). Such a difference
80 critically limits our ability to understand and quantify the impact of convective
81 aggregation on the climate system. Therefore efforts to better characterize the robustness
82 and dependency of self-aggregation to the surface temperature and to better understand
83 the underlying mechanisms recently culminated in the RCE Model Intercomparison
84 Project (RCEMIP, Wing et al., 2018): using a coordinated setup of RCE simulations,
85 RCEMIP aims at clarify the discrepancies between CPMs and GCMs, as well
86 as among the numerous GCMs that took part in the exercise.

87 Even though the mechanisms leading to self-aggregation differ among models, most
88 of them indicate that feedbacks between longwave (LW) radiation, water vapor and clouds
89 (Bretherton et al., 2005; Muller & Held, 2012; Craig & Mack, 2013; Wing & Emanuel,
90 2014; Coppin & Bony, 2015) favors the initiation and maintenance of self-aggregation
91 while the surface flux feedback alternates from being positive in the early stages to being
92 negative later on (Tompkins & Craig, 1998; Wing & Emanuel, 2014; Coppin & Bony,
93 2015; Holloway & Woolnough, 2016; Wing & Cronin, 2016). Other identified processes
94 appear more model-dependent: the relative importance of clear- versus cloudy-sky radiative
95 processes, the relative contribution of direct (adiabatic) or indirect (i.e. through
96 the atmospheric circulation) radiative effects in the evolution of convective aggregation,
97 the role of moist static energy (MSE) horizontal advection and the role of the shallow
98 circulation that develops in a number of CPM simulations between convectively-active
99 and convectively-suppressed regions (Muller & Bony, 2015; Shamekh et al., 2020b).

100 The latter point has been the focus of several studies pointing out the crucial role
101 of either the free troposphere or the boundary layer (BL) in the establishment of this
102 shallow circulation and its potential role in the initiation of convective self-aggregation.
103 Bretherton et al. (2005) find that enhanced radiative cooling in the lower troposphere
104 of the dry regions leads to the formation of a shallow circulation transporting MSE up-
105 gradient, from low-MSE to already high-MSE regions, thereby favoring self-aggregation
106 through the increase of MSE gradients and the MSE variance. This has been confirmed
107 by several CPM studies, although the nature of the radiative feedbacks driving this shallow
108 circulation depends on the model and its configuration. Muller and Bony (2015) suggest
109 that the BL differential radiative cooling rate between dry and moist regions is the
110 main driver. The BL-centric framework of Yang (2018) confirms the key role of BL di-

111 abatic processes and further suggests that an additional buoyancy effect is necessary to
112 establish a horizontal pressure gradient able to drive convective self-aggregation. This
113 hypothesis has been verified by conceptual bulk models for both the dry and moist BL
114 structures (Naumann et al., 2017, 2019), which show that heterogeneous radiative BL
115 cooling is able to produce pressure gradients between areas of strong and weak BL cool-
116 ing. The strength of the induced shallow circulation is comparable to that caused by sur-
117 face temperature differences of a few kelvins, emphasizing the potential first-order effect
118 of spatial differences in BL radiative cooling for self-aggregation.

119 The strength of the shallow circulation has also been linked to the speed of self-
120 aggregation. Using a CPM coupled with interactive SSTs, Shamekh et al. (2020b) un-
121 derline that larger surface pressure anomalies, which result from both BL radiative cool-
122 ing and positive SST anomalies in the dry regions, strongly modulate how fast convec-
123 tion self-aggregates. But, in these simulations with interactive SSTs as well as in those
124 more commonly using fixed SSTs, the larger radiative cooling in the BL and lower tro-
125 posphere strongly depends on the free-tropospheric drying induced by the large-scale deep
126 circulation that emerges with self-aggregation. The respective role and balance between
127 these two circulations in convective self-aggregation remains unclear, as well as how this
128 balance can shift with surface warming. The existence and role of such BL differential
129 radiative cooling and associated shallow circulation has yet to be shown in GCMs.

130 In this paper, we document and investigate the mechanisms responsible for con-
131 vection self-aggregation in the CNRM-CM6-1 GCM (Voldoire et al., 2019; Roehrig et
132 al., 2020). This analysis thus focuses on the equilibrium states reached by the model un-
133 der various SSTs, but also on the paths taken by the model to aggregate convection. For
134 some SSTs, the path involves multiple phases of self-aggregation, with different timescales.
135 After describing the CNRM-CM6-1 model, the experiments performed with it and the
136 diagnostics used to study self-aggregation in Section 2, we investigate the equilibrium
137 states of the model in Section 3. In particular we assess whether different metrics char-
138 acterizing self-aggregation consistently evolve with increasing SST. Section 4 then inves-
139 tigate the transient response and the feedbacks driving the different phases of convec-
140 tion self-aggregation. Section 5 summarizes and discusses our main findings.

2 Methods

2.1 The CNRM-CM6-1 atmospheric component

We use the atmospheric component of the CNRM-CM6-1 climate model (Voldoire et al., 2019), namely the global atmospheric model ARPEGE-Climat 6.3 (Roehrig et al., 2020). This model version contributed to the RCEMIP initiative (Wing et al., 2018, 2020).

ARPEGE-Climat is a spectral model derived from cycle 37 of the ARPEGE/IFS (Integrated Forecast System) numerical weather prediction model developed jointly by Météo-France and the European Center for Medium-range Weather Forecast. It uses a linear triangular truncation T127 with a corresponding reduced Gaussian grid (Hortal & Simmons, 1991). The model horizontal resolution is about 1.4° . Along the vertical the model encompasses 91 vertical levels, following a progressive hybrid σ -pressure coordinate. The first and last model levels are near 10 m and 80 km, respectively, and the vertical resolution ranges from 20 to 200 m in the boundary layer, while being around 400–500 m in the free troposphere.

The dynamical core is based on a two-time level semi-Lagrangian numerical integration scheme. It resolves the vorticity and divergence form of the primitive equations, with temperature and surface pressure logarithm being the thermodynamic state variables. It also computes the advection of specific humidity and eight microphysical species (four for the large-scale microphysics scheme, four for the convection scheme). Horizontal diffusion, which intensity depends on the wave length, the altitude and the diffused variable, is used to stabilize the model and allows, together with the semi-Lagrangian scheme, to keep rather long model time steps (15 minutes).

Longwave radiation calculations follow the GCM version of the Rapid Radiation Transfer Model (Mlawer et al., 1997) while the shortwave radiation calculations are based on the six-band scheme of Fouquart and Bonnel (1980) and Morcrette et al. (2008). The stratiform microphysics scheme treats cloud liquid water, cloud ice crystals, rain and snow, and accounts for autoconversion, sedimentation, icing-melting, precipitation evaporation, and collection processes (Lopez, 2002). The turbulence is solved by the 1.5-order turbulent kinetic energy scheme of (Cuxart et al., 2000) using the mixing length of Bougeault and Lacarrere (1989). Finally, dry, shallow and deep convection regimes are represented using the unified, bulk, mass-flux framework described in Piriou et al. (2018). It follows

172 the ideas of Gueremy (2011) for the convective profile and closure, and those of Piriou
173 et al. (2007) for an explicit separation between the convective vertical transport and the
174 convective microphysical processes. The convective microphysical processes are thus treated
175 in the same way as the large-scale, resolved microphysical processes (Lopez, 2002), con-
176 sidering only that they occur in the convective environment. As a result, convective mi-
177 crophysical species mirror those in the convection environment, thereby allowing entrain-
178 ment and detrainment of the condensates. Entrainment and detrainment processes de-
179 pend on the prognostic updraft vertical velocity and follow the buoyancy sorting approach
180 of Bretherton et al. (2004). The scheme closure is based on the relaxation of the dilute
181 Convective Available Potential Energy.

182 **2.2 RCEMIP simulations**

183 CNRM-CM6-1 is run in the RCE configuration without rotation, following RCEMIP
184 guidelines (Wing et al., 2018): fixed and uniform SSTs of 295 K, 300 K and 305 K, con-
185 stant and uniform incoming solar radiation at the top of atmosphere and zenith angle
186 (551.58 W m^{-2} and 42.05° , respectively). The simulations are uniformly initialized from
187 the equilibrium profiles obtained from single-column experiments with the same model
188 and for the same SSTs. The three CNRM-CM6-1 RCE simulations show different de-
189 grees of convection aggregation as emphasized by the patterns of Column Relative Hu-
190 midity (CRH – ratio of precipitable water to saturated precipitable water) and the ag-
191 gregation indices indicated in Figure 1 (see also Wing et al., 2020).

192 Since the timing and strength of convective self-aggregation may depend on the ini-
193 tial state, we designed ensembles of five simulations for each of the 295-K, 300-K and 305-
194 K SSTs. Each member of the ensemble is initialized with a globally-averaged instantane-
195 ous state taken from the equilibrium phase of the first member at the same SST (i.e.
196 the RCEMIP simulation described above). Besides, in order to further investigate the
197 aggregation sensitivity to SSTs, additional experiments are performed at each SST be-
198 tween 295 K and 305 K by increment of 1 K. All the simulations last three years. The
199 equilibrium values are averages over the last year.

200

2.3 Moist static energy framework

201

202

203

204

205

206

The traditional framework to analyse self-aggregation of deep convection is based on the frozen moist static energy (FMSE), which is conserved under adiabatic processes including the phase change of water. When integrated over the column, its variance increases as convection organizes: the FMSE increases in moist regions and decreases in dry regions. In the CNRM-CM6-1 model, the FMSE h follows the definition of Wing et al. (2018):

207

$$h = c_p T + gz + L_v q_v - L_f q_i \quad (1)$$

208

209

210

211

212

where c_p denotes the specific heat of moist air, T the temperature, g the gravity acceleration, z the geopotential height, L_v and L_f the latent heat of vaporization and fusion at the water triple point, respectively, and q_v and q_i the specific humidity and the ice specific mass, respectively (including convective and large-scale components of cloud ice crystal and precipitating snow).

213

214

215

216

The FMSE range strongly depends on the SST, which renders the comparison of indices or budget based on FMSE difficult for different SSTs. To account for this dependency, we follow Pope et al. (2021) and define the normalized vertically-integrated FMSE \widehat{h}_n between theoretical upper and lower limits using the formula:

217

$$\widehat{h}_n = \frac{\widehat{h} - \widehat{h}_{\min}}{\widehat{h}_{\max} - \widehat{h}_{\min}} \quad (2)$$

218

219

220

221

222

223

224

225

where hats ($\widehat{}$) denote a density-weighted vertical integral, and \widehat{h}_{\min} and \widehat{h}_{\max} the lower and upper limits of \widehat{h} for a given SST, respectively. \widehat{h}_{\min} is defined as the vertically-integrated FMSE of a dry adiabatic profile with zero moisture in the troposphere, plus the integrated FMSE of the initial profile above the tropopause. \widehat{h}_{\max} corresponds to the vertically-integrated FMSE of a fully saturated moist pseudo-adiabatic profile from the surface to the tropopause, plus the integrated FMSE of the initial profile above the tropopause. The tropopause is defined as the lowest level in the initial profile at which the lapse rate decreases below 2 K km^{-1} .

226

227

228

229

To investigate the relative importance of different processes impacting the variance of the normalized vertically-integrated FMSE \widehat{h}_n , we use the same budget equation derived from Wing and Emanuel (2014) but replace the vertically-integrated FMSE \widehat{h} by its normalized counterpart (see also Pope et al., 2021):

230

$$\frac{1}{2} \frac{\partial \widehat{h}_n^2}{\partial t} = \widehat{h}'_n \text{SEF}'_n + \widehat{h}'_n \text{NetSW}'_n + \widehat{h}'_n \text{NetLW}'_n + \widehat{h}'_n \widehat{\nabla_h \cdot (\mathbf{u}h_n)} \quad (3)$$

231 with SEF the surface enthalpy flux (sum of sensible and latent heat fluxes), NetSW and
 232 NetLW the net atmospheric column shortwave (SW) and longwave radiative heating sources,
 233 and $\widehat{\nabla_h \cdot (\mathbf{u}h_n)}$ the vertically-integrated horizontal divergence of the normalized FMSE.
 234 Primes (') denote the local anomalies from the instantaneous domain mean. This enables
 235 us to better compare the strength of the feedbacks driving self-aggregation for different
 236 SSTs.

237 **2.4 Characterization of CRH distributions**

238 The next section compares different aggregation indices used in the literature to
 239 characterize convective aggregation. Because they are not based on the same variables
 240 and correspond to different visions of what an aggregated atmosphere looks like, these
 241 indices often evolve separately with SSTs, or with time for a given SST. In order to bet-
 242 ter analyze these differences and gain a more detailed view of what exactly is changing
 243 in the moisture distribution with self-aggregation, we approximate the CRH spatial prob-
 244 ability distribution function (PDF) by either a unique lognormal distribution or, when
 245 convection is aggregated, by the superimposition of two such distributions, one for each
 246 of the dry and moist modes of CRH. As a result, the CRH distribution, and thereby the
 247 aggregated state, can be characterized with 5 parameters. The analytical form of the ap-
 248 proximated CRH distribution reads:

$$249 \quad f(x) = \frac{1 - \alpha}{x\sigma_d\sqrt{2\pi}} e^{-\frac{(\ln x - \mu_d)^2}{2\sigma_d^2}} + \frac{\alpha}{x\sigma_m\sqrt{2\pi}} e^{-\frac{(\ln x - \mu_m)^2}{2\sigma_m^2}} \quad (4)$$

250 with α , the fraction of the total PDF covered by the moist PDF, and μ_d , μ_m , σ_d and σ_m ,
 251 the expected value (μ) and standard deviation (σ) of the dry and moist lognormal dis-
 252 tributions, respectively.

253 The point where both distributions are equal is called CRH_c . It is used to sepa-
 254 rate dry and moist regions. The best fit for each reconstructed PDF correspond to the
 255 combination of the five parameters that minimizes the quadratic error with the original
 256 PDF. Examples of optimized fits for several days of the 305-K simulation are shown in
 257 Figure S1 (supplemental material).

258 This decomposition of the CRH spatial distribution provides a solid framework to
 259 diagnose how the CRH distribution varies with time or with the SST. Higher expected
 260 value μ corresponds to a broader distribution while higher standard deviation σ means

261 the distribution is more skewed towards one of its extremes (e.g., Text S2 and Figure S2).
 262 In addition to these parameters, we also estimate the CRH value at the peak of each log-
 263 normal distribution (CRH_d and CRH_m for the dry and moist distributions, respectively).

264 **3 Convection self-aggregation equilibrium in CNRM-CM6-1**

265 **3.1 Quantifying the level of convection self-aggregation**

266 While convection is mostly organized along bands of high CRH, the main differ-
 267 ence between SSTs is the larger dry areas and increasing contrasts at high SSTs (Fig-
 268 ure 1). To objectively quantify self-aggregation, a wide range of indices are used in the
 269 literature. Figure 2 illustrates some of those that are easily applicable to coarse-resolution
 270 GCMs for all the explored SST range as well as for all members of the 295-K, 300-K and
 271 305-K ensembles.

272 All indices using vertical integrals of variables associated with humidity, i.e. the
 273 variances of vertically-integrated FMSE ($\text{var}(\hat{h})$) and normalized FMSE ($\text{var}(\hat{h}_n)$), pre-
 274 cipitable water ($\text{var}(\text{PRW})$) and CRH ($\text{var}(\text{CRH})$), show a gradual increase of self-aggregation
 275 with warming, with simulations between 298 K and 301 K having a similar equilibrium.
 276 Since $\text{var}(\hat{h}_n)$ is well correlated with $\text{var}(\text{CRH})$ and $\text{var}(\text{PRW})$, and facilitates the com-
 277 parison of the aggregation mechanisms across SSTs, we now use it as our main index to
 278 quantify convective aggregation.

279 The shallow circulation efficiency η (see appendix A for details) is a dynamical in-
 280 dex which quantifies the fraction of mass transport between dry and moist regions done
 281 by the shallow circulation (Shamekh et al., 2020b). It is highly correlated with $\text{var}(\hat{h}_n)$.
 282 This suggests a direct link between self-aggregation and the strength of the shallow cir-
 283 culation. The variances of normalized FMSE and η are also well correlated with the sur-
 284 face pressure difference between moist and dry regions (Δp_s) and the net radiative boundary-
 285 layer warming difference between moist and dry regions ($\Delta \partial_t T|_{\text{rad}}$, positive when radia-
 286 tive cooling is stronger in the dry regions). The latter difference mainly results from dif-
 287 ferences in the LW clear-sky temperature tendencies (second to last column in Figure 2).
 288 This suggests that, as proposed by Naumann et al. (2017) and Naumann et al. (2019),
 289 this heterogeneous radiative boundary-layer cooling is consistent with positive surface
 290 pressure anomalies in dry regions, which thereby strengthens the shallow circulation. In

291 turn, the latter positively feeds back on self-aggregation as it enhances the FMSE im-
 292 port in moist regions and thus the variance of \hat{h}_n .

293 In contrast to the previous indices, the subsiding fraction (SF), i.e. the fraction of
 294 the domain where subsidence occurs at 500 hPa (noted SF500), as well as those fraction
 295 computed using the 850-hPa vertical velocity (SF850) or the vertically-averaged verti-
 296 cal velocity ($\overline{\text{SF}}$), increase from 295 K to 298-299 K and then decrease up to 305 K, with
 297 a rate depending on the SF index version. This behavior strongly contrasts with the other
 298 indices and indicates that a maximum subsiding fraction does not always relate to max-
 299 imum aggregation as quantified with the \hat{h}_n variance (see also Wing et al., 2020). The
 300 rather high sensitivity of the SF indices to the level used in their calculation questions
 301 the way self-aggregation should be quantified.

302 Because of the bi-modal property of the CRH distribution (e.g., Figure S1 – also
 303 true for \hat{h}_n or PRW), the use of a variance metric can also be questioned. We therefore
 304 explore a more detailed approach to characterize the CRH distribution and its sensitiv-
 305 ity to SSTs (Section 2.4).

306 The weight α of the moist PDF decreases with SST until 298 K and then saturates,
 307 with a distinct minimum at 298-299 K (Figure 3). A similar pattern is found for μ_m and
 308 CRH_m , further emphasized by the strong correlations between these three parameters.
 309 σ_m is also maximum at 298-299 K but decreases back to low-SST levels at higher SST.
 310 This underlines that, for SSTs up to 299 K, the moist component of the CRH distribu-
 311 tion becomes moister and narrower, while its area decreases. For higher SSTs, the dis-
 312 tribution moves back to lower CRH values while maintaining a similar fraction of the
 313 full PDF.

314 In contrast, μ_d and CRH_d decrease with SST and strongly correlate with the nor-
 315 malized FMSE variance $\text{var}(\hat{h}_n)$. Therefore, as SST increases, the dry component of the
 316 CRH distribution becomes drier and narrower. This also indicates that the evolution of
 317 the dry regions is the primary driver of the monotonic FMSE variance increase with SST
 318 (as well as that of the shallow circulation efficiency η), especially above 298-299 K.

319 The distinct maximum of σ_m at 298-299 K and its relationship with $\text{var}(\hat{h}_n)$ mir-
 320 rors that between SF indices and $\text{var}(\hat{h}_n)$ in Figure 2. The high correlation of α with μ_m
 321 and CRH_m also suggests that the moistest regions partly drive the fraction of the do-

322 main covered by subsidence (or large-scale ascent) at equilibrium. The relationship be-
 323 tween SF indices and the moist regions is however more complex and SF indices only weakly
 324 correlate with μ_m and CRH_m (not shown). This hints that SF indices are not fully con-
 325 trolled by the CRH level in moist regions, which thus does not fully drive the large-scale
 326 deep circulation.

327 To summarize, SF indices and α thus characterize self-aggregation as a balance be-
 328 tween moist/convective and dry/subsiding regions and are mainly controlled by the moist
 329 component of the CRH distribution and convection, while $\text{var}(\hat{h}_n)$ and η are primarily
 330 driven by the shape of the moisture distribution, especially its dry component.

331 3.2 Atmospheric vertical structure at equilibrium

332 Convective self-aggregation is generally associated with a drier free troposphere (Bretherton
 333 et al., 2005; Tobin et al., 2012, 2013; Stein et al., 2017). This is true in CNRM-CM6-
 334 1, particularly in the lower free troposphere, below 650 hPa, where relative humidity (RH)
 335 decreases gradually with SST (Figure 4a). This decrease is primarily driven by the dry
 336 regions (Figure S3).

337 The structure of this dry free troposphere varies with SST, from having a single
 338 minimum around 500 hPa at 295 K to having a mostly uniform RH profile with two lo-
 339 cal minima at 800 hPa and 300 hPa at 305 K. The cloud fraction also gradually decreases
 340 with SST between 850 hPa and 300 hPa (Figures 4b and 5). In contrast, the low-level
 341 cloud fraction increases with SST, mainly in the dry regions (Figure S3), with a slight
 342 downward shift from 298 K on.

343 In the upper troposphere, as expected from thermodynamical considerations (Hartmann
 344 & Larson, 2002; Bony et al., 2016), high clouds rise with increasing SST. The high-cloud
 345 fraction decreases from 295 K to 298 K, and then increases from 298 K to 305 K, albeit
 346 at a slower rate. In moist regions, it increases from 295 K to 298 K, then decrease un-
 347 til 305 K (Figure S4), while in dry regions, it mostly decreases (Figure S3, see also 5).
 348 Thus, for high SSTs, the model behavior at global scale contrasts with the high-cloud
 349 fraction decrease with SST predicted by the stability-iris effect (Bony et al., 2016). Al-
 350 though the cloud fraction monotonically reduces in dry regions, convective clouds be-
 351 come thicker in moist regions, possibly also more frequent, thereby compensating the iris
 352 effect contraction of the anvil-type high clouds.

353 In terms of large-scale circulation, Figure 5 emphasizes changes from a large area
 354 of shallow convection at moderate CRH and a strong lower tropospheric subsidence at
 355 low CRH (Figure 5a) to an extended yet weaker subsidence area in the lower troposphere
 356 at moderate CRH, near layers with high low-cloud fractions (Figure 5d). In the moistest
 357 region, the circulation evolves from top-heavy to mid- or bottom-heavy ascents, consis-
 358 tently with the enhancement of the shallow circulation between dry and moist regions.

359 4 Mechanisms leading to convection self-aggregation

360 Whatever the SST, a first phase of convection self-aggregation occurs during the
 361 first 20 days of the simulations (Figure 6a). For SST above approximately 300 K, a sec-
 362 ond phase of self-aggregation involves longer timescales, from about 100 days at 305 K
 363 to 400 days at 300 K. We first focus on the first phase of self-aggregation, common to
 364 all the SSTs explored in the present work.

365 4.1 First phase of convection self-aggregation

366 The mechanisms driving the first phase of self-aggregation are investigated using
 367 the budget of the \hat{h}_n variance (Equation 3) to highlight the involved feedbacks (Figure
 368 7, see also Figure S5 for the separation between clear- and cloudy-sky feedbacks).

369 At all SSTs, the initial self-aggregation is driven by the LW cloud feedback, with
 370 an additional contribution, yet weaker from the latent heat flux feedback. The latter de-
 371 creases with SST and, after a few days, becomes negative. The SW and LW clear-sky
 372 feedbacks also contribute to enhance self-aggregation, though with a slight delay. The
 373 amplitude of the surface flux and SW feedbacks is larger at 295 K and 300 K than at
 374 305 K, which likely explains why convection self-aggregates slightly faster at these SSTs.
 375 The sensible heat flux feedback is always positive and weak, and slightly larger at low
 376 SSTs. Finally, the advection feedback is always negative, except around day 10 at 305
 377 K. Its intensity slightly increases with SSTs. Though the feedback amplitude varies with
 378 SSTs, their time evolution over the first 20 days and their relative contribution are mostly
 379 similar across SSTs. Therefore, we investigate hereafter the 295-K simulation in more
 380 detail to identify the regions where the feedbacks are the most active (Figure 8). Sim-
 381 ilar diagnostics for 300 K and 305 K are provided in Figures S6 and S7.

382 Following 2-3 days of spin-up, convection rapidly self-aggregates between days 5
 383 and 10 (black line on Figure 8). The diabatic feedback, dominated by the cloudy-sky long-
 384 wave feedback, is maximum in the dry regions (Figures 8c and S8). The shortwave (mostly
 385 its clear-sky component, see Figure S8) and the surface flux feedbacks in the dry regions
 386 also weakly contributes when self-aggregation starts. In contrast, the advection feedback
 387 is mostly negative, except in the driest and moistest regions.

388 This first phase results in a rapid initial drying visible in CRH and precipitable wa-
 389 ter (black lines in Figure 9a,e, respectively) and the apparition of a relatively low pro-
 390 portion of very dry columns.

391 At 295 K, the CRH distribution stops evolving after the first 15 days. For SSTs
 392 above approximately 300 K, a second phase of self aggregation occurs. The CRH dis-
 393 tribution becomes fully bi-modal as the proportion of dry columns increases and becomes
 394 similar to or larger than that of their moist counterpart.

395 **4.2 Second phase of convection self-aggregation**

396 When it exists, the second phase of self-aggregation, which ends when the simu-
 397 lation reaches its final equilibrium given in Figure 2, involves much longer timescales than
 398 the first phase of self-aggregation (Figure 6). It is characterized by the progressive dry-
 399 ing of the free troposphere (Figure 10a-d), particularly in the dry regions (not shown).

400 The second phase of aggregation consists in a first period when aggregation indices
 401 remain approximately constant (Figure 6). It is shorter at high SSTs. It is followed by
 402 a second period during which self-aggregation accelerates until its final equilibrium. This
 403 acceleration is more pronounced at high SSTs. At the same time, the moist region weight
 404 α in the CRH distribution decreases rapidly, σ_d increases, σ_m remains approximately con-
 405 stant and μ_m and μ_d both decrease (Figures 6d,h-k). Thus the dry component of the CRH
 406 distribution weights more and gets more skewed towards drier regimes, while its moist
 407 component concentrates more around high CRH, getting only slightly moister (see also
 408 Figure 9a-d).

409 We now focus on the 305-K simulation where the increase in aggregation speeds
 410 up around days 50-70 (Figure 6) and compare it with the 295 K simulation where this
 411 transition phase is absent. Results are similar for SSTs above 300 K, except that the tran-

412 sition takes more time (up to 400 days for 300 K). The early time of the transition in
 413 the 305-K simulation (days 20-50) is characterized by adjustments within the low and
 414 mid free troposphere, which reduces the geopotential disequilibrium between the moist
 415 and dry regions achieved after the first phase of self aggregation (Figure 6e-f). These ad-
 416 justments in the 305-K simulation are not continuous and involves transient events with
 417 timescales of a few days. It also weakly impacts the CRH distribution (Figure 6d,h-k).

418 Then, from day 50, σ_d sharply increases, μ_d (and CRH_d , not shown) sharply de-
 419 creases, while μ_m decreases at a much more slower pace. This emphasizes the driving
 420 role of the dry regions in initiating the second self-aggregation phase. The delayed in-
 421 crease of precipitable water in the moist regions is also consistent (Figure 9h). The tran-
 422 sition is concomitant with the slow strengthening of the shallow circulation, which be-
 423 comes as intense as the deep circulation near day 70 ($\eta = 0.5$, Figure 6b). This change
 424 in the large-scale overturning circulation is further illustrated in Figure 11 in a CRH rank-
 425 altitude diagram (following Bretherton et al., 2005, see appendix A for the streamfunc-
 426 tion computation). Compared to 295 K where the streamfunction is maximum in the
 427 upper troposphere and does not vary after the initial 20-day self-aggregation, the stream-
 428 function at 305 K evolves from a top-heavy circulation, similar to that at 295 K, albeit
 429 weaker, to a more bottom-heavy circulation, especially after 150 days. The shallow cir-
 430 culation is clearly visible, mostly confined near the margins of moist convective regions.
 431 At 295 K, a shallow circulation similarly exists but remains weak compared to the deep
 432 one.

433 The shallow circulation continuously strengthens from day 20 onwards in the 305-
 434 K simulation, consistently with the increase of the boundary-layer geopotential height
 435 and surface pressure differences between dry and moist regions (Figures 6g,m) and the
 436 opposite trend, albeit weaker, in the low and mid troposphere (Figures 6e-f). Around
 437 day 60-70, self-aggregation accelerates, at the same time when the shallow circulation
 438 efficiency η exceeds 0.5 (Figure 6b), that is when the shallow circulation becomes stronger
 439 than its deep counterpart. This is also true at 302 K (around day 150) and 300 K (around
 440 day 400), while it clearly does not append at 295 K. The acceleration also coincides with
 441 a period of time when moist convective regions become less mobile on average over the
 442 globe, with convection suddenly staying over the same area for 10 to 20 days (Figure 6c,
 443 see appendix B for the diagnostic computation). The enhanced shallow circulation ef-
 444 ficiency is likely able to support a positive net import of FMSE within moist regions thereby

445 favoring their maintenance at the same location for longer time periods (e.g., Raymond
446 et al., 2009).

447 **4.3 Feedback analysis of the second self-aggregation phase**

448 To further understand the processes at play during the second phase of self-aggregation,
449 we now analyze the feedbacks involved in the \hat{h}_n variance budget at 305 K (Figures 12
450 and 13). Similar results, but with different timings, are found for SSTs above 300 K (e.g.,
451 Figure S9 for 302 K).

452 After the initial phase of self-aggregation, most feedbacks do not evolve much, es-
453 pecially between day 20 and day 50. Then, from day 60, while the feedback magnitudes
454 remain similar, except for the advection feedback, the CRH ranks they impact vary. The
455 LW radiation positive feedback, which remains the dominant positive feedback, mostly
456 occur in moderately-dry CRH columns, thus close to the margins of the moist convectively-
457 active regions. It also remain significant, yet weaker, in the driest regions. This LW feed-
458 back is mainly driven by its cloudy-sky component (Figure 13b,e). In contrast, the SW
459 (mostly its clear-sky component), sensible heat flux and latent heat flux feedbacks do
460 not evolve much over the second phase period (Figures 12b,d-e and 13a,d).

461 Finally, the advection feedback is strongly modified during the self-aggregation ac-
462 celeration. From day 60, it becomes positive in the driest columns, significantly impact-
463 ing at day 110 about one third of the domain. There, its positive vertical component dom-
464 inates its negative horizontal counterpart (Figures 13c,f). The opposite occurs in the tran-
465 sition zone between dry and moist regions (around the grey line on Figures 12 and 13),
466 where the negative horizontal advection feedback dominates. On average over the whole
467 domain, the advection feedback is weak, which thus allows the positive LW feedback to
468 enhance self-aggregation during this second phase. This contrasts with what occurs dur-
469 ing the first 60 days, when the vertical and horizontal advection feedbacks are mostly
470 collocated: the total advection feedback is significantly negative and can partly coun-
471 terbalance the positive LW feedback. The adjustment of the circulation thus drives a spa-
472 tial decoupling between the deep and shallow circulations, which is key to weaken glob-
473 ally the negative advection feedback and constrain its negative values to remain close
474 to the moist regions. This thereby allows the positive LW feedback to further increase
475 self-aggregation. In the dry regions, the positive vertical advection feedback further en-

476 hance self-aggregation, most probably through the further drying of the atmospheric columns
 477 (see also Figure 9).

478 **4.4 Sensitivity of the second self-aggregation phase processes to SST**

479 The previous sections suggest an important role of the shallow circulation strength-
 480 ening during the second self-aggregation phase. Therefore, we now analyze the poten-
 481 tial temperature budget contrast between dry and moist regions, to better understand
 482 which process might explain its sensitivity to SST. Figures 14 and 15 show the detail of
 483 the potential temperature budget in dry and moist regions, respectively, as a function
 484 of the degree of self-aggregation (variance of \hat{h}_n), for the 295-K, 300-K, 302-K and 305-
 485 K simulations, and for three layers of the atmospheric column, namely the boundary-
 486 layer (1000-925 hPa), the lower free troposphere (850-700 hPa) and the mid free tropo-
 487 sphere (600-400 hPa). The layers are chosen according to the tendency vertical profiles,
 488 but the following results weakly depends on the exact pressure levels chosen to define
 489 these layers.

490 After the first phase of self-aggregation in the 305-K simulation, all tendencies in
 491 the dry regions remain approximately constant, except within the boundary layer (Fig-
 492 ure 14). As convection continues to self-aggregate, the boundary-layer heating by tur-
 493 bulent processes increases and is slightly enhanced by the weakly increasing cloudy-sky
 494 LW radiative heating, and weakened by the increasing cooling by convective and large-
 495 scale microphysical processes (i.e. condensation and evaporation). The total effect of di-
 496 abatic processes is balanced by a weak, slightly increasing, advective cooling. The bound-
 497 ary-layer potential temperature budget thus depicts an increased mixing within the bound-
 498 ary layer, most probably due to both an increased of the buoyancy surface flux and the
 499 free troposphere air entrainment at the boundary-layer top, together with more low-level
 500 cloudiness at its top (see also Figure 11) and enhanced evaporation of weakly-precipitating
 501 cumulus or stratocumulus.

502 In contrast, in the boundary layer of the wet regions (Figure 15k-o), the turbulent
 503 and cloudy-sky LW radiative heating rates weakly evolve after the first self-aggregation
 504 phase, while the heating by convective and large-scale condensation significantly increases.
 505 It is slightly reinforced by the reducing clear-sky LW radiative cooling. Above, the po-
 506 tential temperature budget is mainly controlled by the convection and large-scale mi-

507 crophysical heating, which is consistent with diabatic heating profiles becoming more bottom-
508 heavy. This is counterbalanced by the advective cooling. Thus, the boundary-layer tem-
509 perature contrast evolution, thereby generating geopotential horizontal gradients which
510 can enhance the shallow circulation (Figure 6b,g,m), mostly rely on turbulent processes
511 within dry regions and convection or large-scale condensation within moist regions. Above,
512 in the lower and mid free troposphere, the increasing condensational heating in moist
513 regions also favors the strengthening of the shallow circulation upper branch.

514 Nevertheless, after the first self-aggregation phase, most potential temperature ten-
515 dencies approximately follow the same trajectory across the four SSTs displayed on Fig-
516 ures 14 and 15, with only a few exceptions. The clear-sky LW radiative tendency within
517 dry regions exhibits a clear sensitivity to SST at the end of the first self-aggregated state.
518 In the free troposphere, the advective tendency mostly mirrors this clear-sky LW radia-
519 tive tendency, consistently with a large-scale subsidence mostly driven by radiative pro-
520 cesses. In the boundary layer, turbulent mixing processes partially compensate the desta-
521 bilization of the lower part of the column by clear-sky LW radiative cooling.

522 As a result, the following picture of the second self-aggregation phase is suggested.
523 After the first phase of self-aggregation, higher SSTs drives higher LW radiative cool-
524 ing in the dry regions, both within the boundary layer and mid free troposphere (around
525 600-400 hPa). In the boundary layer, though the destabilization increased by radiative
526 processes is partially balanced by an enhanced turbulent mixing, the temperature con-
527 trast with moist regions enhances the dry-to-moist region pressure gradient and thus the
528 lower branch of the shallow and deep circulations. Above, the enhanced radiative cool-
529 ing strengthens the large-scale subsidence, drying further the free troposphere and thereby
530 providing a drier environment for convective updrafts. Their dilution is enhanced at up-
531 per levels, which thus leads to more bottom-heavy diabatic heating profiles. This fur-
532 ther enhances the shallow circulation, driving a positive feedback on deep convection.
533 As convective/moist regions become less mobile, radiative feedbacks can reinforce their
534 local effect, i.e. enhancing the drying effect of the radiatively-driven large-scale subsi-
535 dence and enhancing the boundary-layer pressure gradient between dry and moist re-
536 gions. This occurs until a new equilibrium is achieved. Cloud processes further feeds back
537 positively during this second phase of self-aggregation.

538 **5 Conclusions and discussions**

539 In this study, we investigate convective self-aggregation in the CNRM-CM6-1 gen-
 540 eral circulation model and assess its dependence to sea surface temperature (SST) in the
 541 non-rotating radiative-convective equilibrium (RCE) framework as defined within the
 542 RCEMIP exercise (Wing et al., 2018). We use the three simulations run for this project
 543 (homogeneous SST of 295, 300 and 305 K), supplemented by 5-member ensembles at the
 544 RCEMIP SSTs and additional experiments exploring intermediate SSTs between 295 K
 545 and 305 K. In all numerical experiments, self-aggregation occurs within the first 20 days,
 546 at a slightly faster pace at lower SST. As SST increases, the self-aggregated equilibrium
 547 gets drier, and the large-scale circulation between dry and moist regions exhibits a strength-
 548 ening shallow component. Low-cloud cover also increases, mostly in the dry regions. As
 549 expected from thermodynamical arguments, the top of high clouds rises with increas-
 550 ing SSTs. In contrast to the iris effect found with other models (Bony et al., 2016), high-
 551 cloud fraction does not exhibit any clear monotonic shrinking tendency with increasing
 552 SSTs, except below 298 K. High-cloud fraction does diminish in dry region, but high clouds
 553 become thicker or more frequent in moist convectively-active regions. This behavior may
 554 be consistent with the high equilibrium sensitivity in the CNRM-CM6-1 and the role of
 555 cloudy-sky longwave feedbacks in driving it (Saint-Martin et al., 2021), as a weak or ab-
 556 sent iris effect as found here would remove a negative feedback on the climate system.

557 For all experimented SSTs, CNRM-CM6-1 exhibits a rapid initial phase of self-aggregation
 558 similar to that found in other models (e.g., Wing et al., 2017): it primarily involves pos-
 559 itive radiative feedbacks, especially in the cloudy-sky longwave and clear-sky shortwave
 560 components. At the lowest SSTs, the latent heat flux feedback also favors self-aggregation
 561 initiation, but rapidly becomes a strongly negative feedback. Sensible heat fluxes only
 562 marginally contribute to self-aggregation at all SSTs, slightly more at colder SSTs. The
 563 use of the normalized frozen moist static energy framework of Pope et al. (2021) allows
 564 us to more appropriately compare the weights of the various self-aggregation feedbacks
 565 at different SSTs. It emphasizes that the clear-sky shortwave and surface enthalpy flux
 566 feedbacks are notably weaker at 305 K than at lower SSTs. The stronger feedbacks at
 567 low SSTs is thus consistent with a faster initial self-aggregation.

568 Following this first phase of self-aggregation, simulations with surface temperature
 569 above approximately 300 K exhibits a second transition towards a new state of self-aggregation.

570 This transition is slower, lasting from 150 days at 305 K to more than a year at 300 K.
571 At the beginning of this new transition, a first adjustment of the large-scale geopotential
572 horizontal gradients between moist and dry regions, and thus of the associated circulation,
573 occurs, mostly within the mid-troposphere. Its origin remains so far elusive and
574 requires further work in the future. Then, a progressive shift from a top-heavy circulation
575 to a more bottom-heavy circulation occurs. This clearly does not happen at low SSTs.
576 Thus, at high SSTs, a shallow circulation settles and become even more efficient than
577 its deep counterpart. The degree at which self-aggregation stabilizes seems in particular
578 related to the relative importance between the shallow and the deep circulations (the
579 η metric). The speed of this second phase of self-aggregation also appears connected to
580 that of the shallow circulation efficiency enhancement, similarly to what is found in Shamekh
581 et al. (2020b).

582 The second phase of self-aggregation occurs simultaneously to several notable changes.
583 As mentioned above, a shallow circulation settles and becomes stronger than the deep
584 circulation. Convective moist regions become less mobile. Dry regions get significantly
585 drier and occupy wider areas, while moist regions only marginally get moister. Positive
586 advection feedbacks appears in the driest regions. The occurrence of this second phase
587 seems primarily driven by clear-sky radiative processes in dry regions, both within the
588 boundary layer and the mid free troposphere. As discussed in Naumann et al. (2017, 2019)
589 and Shamekh et al. (2020a) and Yang (2018), the enhanced differential radiative cooling
590 in the boundary layer at higher SSTs increases the pressure gradient between dry
591 and moist regions, which thus strengthens the lower branch of the shallow and deep
592 circulations. Above, in the dry regions neighboring moist regions, the enhanced radiative
593 cooling enhances the large-scale subsidence, drying further the free troposphere, and thereby
594 providing a drier environment for convective updrafts. Their dilution is likely enhanced
595 at mid and upper levels, thereby leading to more bottom-heavy diabatic heating profiles.
596 This further enhances the shallow circulation, which positively feed backs on deep con-
597 vection. Besides, the fact that convection is less mobile allows the strengthening of all
598 previous mechanisms, as they can act on the same place for a longer period of time. Cloud
599 processes also act as another positive feedback during this transition. This schematic re-
600 mains an hypothesis, albeit consistent with the diagnostics provided in this manuscript.
601 It will be further tested in the future through dedicated experiments.

602 In addition to more classical metrics of self-aggregation, we propose in this work
 603 a more detailed framework to characterize the CRH spatial distribution and its tempo-
 604 ral evolution: the CRH distribution, when bi-modal, can be well approximated by two
 605 log-normal distributions describing the properties of the dry and moist regions. The as-
 606 sociated diagnostics emphasize that transition to self-aggregation and self-aggregated states
 607 in CNRM-CM6-1 is mostly driven by adjustments within the dry regions, both in terms
 608 of level of dryness and of covered area. Applying these diagnostics to the RCEMIP en-
 609 semble might help better link self-aggregation levels and the CRH distribution and un-
 610 derstand why self-aggregation usually increases with SST in GCMs but not necessarily
 611 in CPMs.

612 Finally, the long timescale of self-aggregation in CNRM-CM6-1 (150 to 400 days
 613 depending on SSTs) questions the way GCM and CPM RCE simulations are compared,
 614 as within the RCEMIP framework. GCMs are run over about 3 years while CPM sim-
 615 ulations only last 100 days. The latter may not be enough to achieve equilibrium and
 616 may explain some of the strong differences between GCM and CPM RCE states and their
 617 sensitivity to SSTs. This calls for further investigation in the future, to assess whether
 618 CNRM-CM6-1 has a peculiar, unusual behavior or CPMs do further self-aggregate on
 619 longer timescales.

620 Appendix A

621 In this paper, the large-scale circulation is characterized through the streamfunc-
 622 tion within a rank of CRH–pressure plan. To compute the streamfunction Ψ , the 32768
 623 columns are ordered from the lowest to the highest CRH and averaged by groups of 32
 624 columns. The 1016 groups of columns are given an index $i = 1, 2, \dots, 1024$. Then, Ψ
 625 is calculated as a horizontal integral of the vertical velocity averaged over each of these
 626 groups, starting from the driest column ($i = 1$):

$$627 \quad \Psi_i(z) = \Psi_{i-1}(z) + w_i(z)\bar{\rho}(z) \quad (\text{A1})$$

628 with $\Psi_{i=0}(z) = 0$ for all z , w the vertical velocity and $\bar{\rho}$ the mean density profile. Thus,
 629 $\Psi_i(z)$ can be interpreted as the net upward mass flux at height z accumulated over the
 630 i driest blocks.

631 The vertical structure of the streamfunction shows two cells: a shallow circulation
 632 with a maximum below 750 hPa and a deeper cell with a maximum above 500 hPa. To

633 calculate the contribution of the shallow circulation to the total circulation (shallow +
 634 deep), Shamekh et al. (2020b) define the circulation efficiency η as:

$$635 \quad \eta = \frac{\Psi_{\max} - \Psi_{\min}}{\Psi_{\max, \text{deep}} + \Psi_{\max} - \Psi_{\min}} \quad (\text{A2})$$

636 with Ψ_{\max} , the maximum of the shallow circulation, $\Psi_{\max, \text{deep}}$, the maximum of the deep
 637 circulation and Ψ_{\min} , the local streamfunction minimum between them.

638 The numerator is the net boundary-layer mass divergence out of dry regions into
 639 moist regions, which returns to the dry regions below the height of the minimum, around
 640 600 hPa. The denominator quantifies the overall large-scale circulation strength, mea-
 641 sured by the total mass transport from dry to moist regions. Thus η (between 0 and 1)
 642 measures the fraction of mass transport from dry to moist regions performed by the shal-
 643 low circulation.

644 Appendix B

645 To quantify how much moist/convectively-active regions are mobile, we calculate
 646 the correlation between the CRH map of a given day and that of each of the following
 647 days (noted ρ_{CRH}). We then identify the lead time (in days) when the correlation goes
 648 below 0.5 (noted $d(\rho_{\text{CRH}}=0.5)$). This quantifies how long the CRH map remains approx-
 649 imately similar. Results remains qualitatively similar when using precipitable water or
 650 correlation thresholds of 0.3 and 0.8.

651 Open Research

652 Hourly output of the 295-K, 300-K and 305-K RCEMIP CNRM-CM6-1 simulations
 653 are part of the RCEMIP dataset, publicly available at [http://hdl.handle.net/21.14101/
 654 d4beee8e-6996-453e-bbd1-ff53b6874c0e](http://hdl.handle.net/21.14101/d4beee8e-6996-453e-bbd1-ff53b6874c0e). Daily output for the 295–305-K RCEMIP-
 655 style simulations and for each member of the 295-K, 300-K and 305-K ensembles, used
 656 in the present paper, are publicly available at [https://thredds-su.ipsl.fr/thredds/
 657 catalog/rcemip/catalog.html](https://thredds-su.ipsl.fr/thredds/catalog/rcemip/catalog.html). A permanent identifier will be created if the present
 658 paper is accepted. Hourly output for the 302-K RCEMIP-style simulation, the ARPEGE-
 659 Climat software (Version 6.3) used for running the simulations, and the scripts used in
 660 the analysis are available upon request to the corresponding author.

661 **Acknowledgments**

662 This project has received funding from the European Union’s Horizon 2020 research and
 663 innovation programme under grant agreement No 820829. We thanks the German Cli-
 664 mate Computing Center (DKRZ) for hosting the standardized RCEMIP data.

665 **References**

- 666 Becker, T., & Stevens, B. (2014). Climate and climate sensitivity to changing CO₂
 667 on an idealized land planet. *Journal of Advances in Modeling Earth Systems*,
 668 *6*, 513–526. doi: 10.1002/2014MS000369
- 669 Becker, T., Stevens, B., & Hohenegger, C. (2017). Imprint of the convective pa-
 670 rameterization and sea-surface temperature on large-scale convective self-
 671 aggregation. *Journal of Advances in Modeling Earth Systems*, *9*. doi:
 672 10.1002/2016MS000865
- 673 Becker, T., & Wing, A. A. (2020). Understanding the Extreme Spread in Climate
 674 Sensitivity within the Radiative-Convective Equilibrium Model Intercompar-
 675 ison Project. *Journal of Advances in Modeling Earth Systems*, *12*(10). doi:
 676 10.1029/2020MS002165
- 677 Bellenger, H., Duvel, J. P., Lengaigne, M., & Levan, P. (2009). Impact of organized
 678 intraseasonal convective perturbations on the tropical circulation. *Geophysical*
 679 *Research Letters*, *36*(16), 1–5. doi: 10.1029/2009GL039584
- 680 Bony, S., Stevens, B., Coppin, D., Becker, T., Reed, K. A., Voigt, A., & Medeiros,
 681 B. (2016). Thermodynamic control of anvil cloud amount. *Proceedings of*
 682 *the National Academy of Sciences of the United States of America*, *113*(32),
 683 8927–8932. doi: 10.1073/pnas.1601472113
- 684 Bougeault, P., & Lacarrere, P. (1989). Parameterization of orography-induced turbu-
 685 lence in a mesobeta-scale model. *Monthly weather review*, *117*(8), 1872–1890.
 686 doi: 10.1175/1520-0493(1989)117(1872:POOITI)2.0.CO;2
- 687 Bretherton, C. S., Blossey, P. N., & Khairoutdinov, M. (2005). An energy-balance
 688 analysis of deep convective self-aggregation above uniform SST. *Journal of the*
 689 *Atmospheric Sciences*, *62*(12), 4273–4292. doi: 10.1175/JAS3614.1
- 690 Bretherton, C. S., McCaa, J. R., & Grenier, H. (2004). A new parameterization
 691 for shallow cumulus convection and its application to marine subtropical
 692 cloud-topped boundary layers. Part I: Description and 1D results. *Monthly*

- 693 *Weather Review*, 132(4), 864–882. doi: 10.1175/1520-0493(2004)132<0864:
 694 ANPFSC>2.0.CO;2
- 695 Coppin, D., & Bellon, G. (2019a). Physical Mechanisms Controlling the Offshore
 696 Propagation of Convection in the Tropics: 1. Flat Island. *Journal of Advances
 697 in Modeling Earth Systems*, 11(9), 3042–3056. doi: 10.1029/2019MS001793
- 698 Coppin, D., & Bellon, G. (2019b). Physical Mechanisms Controlling the Offshore
 699 Propagation of Convection in the Tropics: 2. Influence of Topography. *Jour-
 700 nal of Advances in Modeling Earth Systems*, 11(10), 3251–3264. doi: 10.1029/
 701 2019MS001794
- 702 Coppin, D., & Bony, S. (2015). Physical mechanisms controlling the initia-
 703 tion of convective self-aggregation in a General Circulation Model. *Jour-
 704 nal of Advances in Modeling Earth Systems*, 7, 2060–2078. doi: 10.1002/
 705 2015MS000571
- 706 Coppin, D., & Bony, S. (2017). Internal variability in a coupled general circula-
 707 tion model in radiative-convective equilibrium. *Geophysical Research Letters*,
 708 44(10), 5142–5149. doi: 10.1002/2017GL073658
- 709 Coppin, D., & Bony, S. (2018). On the Interplay Between Convective Aggregation,
 710 Surface Temperature Gradients, and Climate Sensitivity. *Journal of Advances
 711 in Modeling Earth Systems*, 10(12), 3123–3138. doi: 10.1029/2018MS001406
- 712 Craig, G. C., & Mack, J. M. (2013). A coarsening model for self-organization of
 713 tropical convection. *Journal of Geophysical Research Atmospheres*, 118(16),
 714 8761–8769. doi: 10.1002/jgrd.50674
- 715 Cronin, T. W., & Wing, A. A. (2017). Clouds, Circulation, and Climate Sensitivity
 716 in a Radiative-Convective Equilibrium Channel Model. *Journal of Advances in
 717 Modeling Earth Systems*, 9(8), 2883–2905. doi: 10.1002/2017MS001111
- 718 Cuxart, J., Bougeault, P., & Redelsperger, J. L. (2000). A turbulent scheme allowing
 719 for mesoscale and large-eddy simulations. *Quarterly Journal of the Royal Me-
 720 teorological Society*, 130(604), 3055–3079. doi: 10.1256/qj.03.130
- 721 Fouquart, Y., & Bonnel, B. (1980). Computations of solar heating of the Earth’s
 722 atmosphere—A new parameterization. *Beiträge zur Phys der Atmosphäre*, 53,
 723 35–62.
- 724 Gueremy, J. F. (2011). A continuous buoyancy based convection scheme: One-
 725 and three-dimensional validation. *Tellus, Series A: Dynamic Meteorology and*

- 726 *Oceanography*, 63(4), 687–706. doi: 10.1111/j.1600-0870.2011.00521.x
- 727 Hartmann, D. L., & Larson, K. (2002). An important constraint on tropical cloud
 728 - climate feedback. *Geophysical Research Letters*, 29(20), 12-1-12-4. doi:
 729 https://doi.org/10.1029/2002GL015835
- 730 Hohenegger, C., & Stevens, B. (2018). The role of the permanent wilting point in
 731 controlling the spatial distribution of precipitation. *Proceedings of the National
 732 Academy of Sciences of the United States of America*, 115(22), 5692–5697. doi:
 733 10.1073/pnas.1718842115
- 734 Holloway, C. E., Wing, A. A., Bony, S., Muller, C., Masunaga, H., L’Ecuyer, T. S.,
 735 ... Zuidema, P. (2017). Observing Convective Aggregation. *Surveys in
 736 Geophysics*, 38(6), 1199–1236. doi: 10.1007/s10712-017-9419-1
- 737 Holloway, C. E., & Woolnough, S. J. (2016). The sensitivity of convective ag-
 738 gregation to diabatic processes in idealized radiative-convective equilibrium
 739 simulations. *Journal of Advances in Modeling Earth Systems*, 8, 166–195. doi:
 740 10.1002/2016MS000625
- 741 Hortal, M., & Simmons, A. J. (1991). Used of Reduced Gaussian Grids in Spectral
 742 Models. *Monthly Weather Review*, 119, 1057–1074. doi: 10.1175/1520-
 743 -0493(1991)119(1057:UORGGI)2.0.CO;2
- 744 Houze, R. A. (2004). Mesoscale convective systems. *Reviews of GeophysicsGeo-
 745 physics*, 104, 237–286. doi: 10.1016/B978-0-12-374266-7.00009-3
- 746 Khairoutdinov, M., & Emanuel, K. (2013). Rotating radiative-convective equilibrium
 747 simulated by a cloud-resolving model. *Journal of Advances in Modeling Earth
 748 Systems*, 5(4), 816–825. doi: 10.1002/2013MS000253
- 749 Kiladis, G. N., Wheeler, M. C., Haertel, P. T., Straub, K. H., & Roundy, P. E.
 750 (2009). Convectively coupled equatorial waves. *Reviews of Geophysics*, 47(2),
 751 1–42. doi: 10.1029/2008RG000266
- 752 Lopez, P. (2002). Implementation and validation of a new prognostic large-scale
 753 cloud and precipitation scheme for climate and data-assimilation purposes.
 754 *Quarterly Journal of the Royal Meteorological Society*, 128(579), 229–257. doi:
 755 10.1256/00359000260498879
- 756 Madden, R. A., & Julian, P. R. (1994). Observations of the 40-50-day tropical os-
 757 cillation - a review. *Monthly Weather Review*, 122(5), 814–837. doi: 10.1175/
 758 1520-0493(1994)122(0814:OOTDTC)2.0.CO;2

- 759 Mlawer, E. J., Taubman, S. J., Brown, P. D., Iacono, M. J., & Clough, S. A.
 760 (1997). Radiative transfer for inhomogeneous atmospheres: RRTM, a vali-
 761 dated correlated-k model for the longwave. *Journal of Geophysical Research*
 762 *Atmospheres*, *102*(14), 16663–16682. doi: 10.1029/97jd00237
- 763 Morcrette, J.-J., Barker, H. W., Cole, J. N. S., Iacono, M. J., & Pincus, R. (2008).
 764 Impact of a New Radiation Package, McRad, in the ECMWF Integrated
 765 Forecasting System. *Monthly Weather Review*, *136*(12), 4773–4798. doi:
 766 10.1175/2008MWR2363.1
- 767 Muller, C. J., & Bony, S. (2015). What favors convective aggregation and
 768 why? *Geophysical Research Letters*, *42*(13), 5626–5634. doi: 10.1002/
 769 2015GL064260
- 770 Muller, C. J., & Held, I. M. (2012). Detailed investigation of the self-aggregation
 771 of convection in cloud-resolving simulations. *Journal of the Atmospheric Sci-*
 772 *ences*, *69*(8), 2551–2565. doi: 10.1175/JAS-D-11-0257.1
- 773 Naumann, A. K., Stevens, B., & Hohenegger, C. (2019). A moist conceptual model
 774 for the boundary layer structure and radiatively driven shallow circulations
 775 in the trades. *Journal of the Atmospheric Sciences*, *76*(5), 1289–1306. doi:
 776 10.1175/JAS-D-18-0226.1
- 777 Naumann, A. K., Stevens, B., Hohenegger, C., & Mellado, J. P. (2017). A con-
 778 ceptual model of a shallow circulation induced by prescribed low-level radia-
 779 tive cooling. *Journal of the Atmospheric Sciences*, *74*(10), 3129–3144. doi:
 780 10.1175/JAS-D-17-0030.1
- 781 Piriou, J. M., Guérémy, J. F., & Bouteloup, Y. (2018). *A subgrid convection*
 782 *scheme for representing dry, moist and precipitating convection in large-*
 783 *scale models, PCMT. Part 1: equations* (Tech. Rep. No. 32). Toulouse,
 784 France: CNRM. Retrieved from [http://www.umr-cnrm.fr/IMG/pdf/](http://www.umr-cnrm.fr/IMG/pdf/gueremy_part1_note-cnrm_f.pdf)
 785 [gueremy_part1_note-cnrm_f.pdf](http://www.umr-cnrm.fr/IMG/pdf/gueremy_part1_note-cnrm_f.pdf)
- 786 Piriou, J. M., Redelsperger, J. L., Geleyn, J. F., Lafore, J. P., & Guichard, F.
 787 (2007). An approach for convective parameterization with memory: Separating
 788 microphysics and transport in grid-scale equations. *Journal of the Atmospheric*
 789 *Sciences*, *64*(11), 4127–4139. doi: 10.1175/2007JAS2144.1
- 790 Pope, K. N., Holloway, C. E., Jones, T. R., & Stein, T. H. M. (2021). Cloud-
 791 radiation interactions and their contributions to convective self-aggregation.

- 792 *Journal of Advances in Modeling Earth Systems*, 13(9), e2021MS002535. doi:
793 10.1029/2021MS002535
- 794 Popke, D., Stevens, B., & Voigt, A. (2013). Climate and climate change in a
795 radiative-convective equilibrium version of ECHAM6. *Journal of Advances*
796 *in Modeling Earth Systems*, 5(1), 1–14. doi: 10.1029/2012MS000191
- 797 Raymond, D. J., Sessions, S. L., Sobel, A. H., & Fuchs, Ž. (2009). The Mechanics of
798 Gross Moist Stability. *Journal of Advances in Modeling Earth Systems*, 1(3).
799 doi: 10.3894/JAMES.2009.1.9
- 800 Roehrig, R., Beau, I., Saint-Martin, D., Alias, A., Decharme, B., Guérémy, J. F., ...
801 Sénési, S. (2020). The CNRM Global Atmosphere Model ARPEGE-Climat 6.3:
802 Description and Evaluation. *Journal of Advances in Modeling Earth Systems*,
803 12(7), 1–53. doi: 10.1029/2020MS002075
- 804 Rotunno, J., Klemp, J. B., & Weisman, M. L. (1988). A theory for Strong, Long-
805 Lived Squall Lines. *Journal of Atmospheric Sciences*, 45(3), 463–485. doi: 10
806 .1175/1520-0469(1988)045<0463:ATFSSL>2.0.CO;2
- 807 Saint-Martin, D., Geoffroy, O., Voldoire, A., Cattiaux, J., Brient, F., Chauvin, F.,
808 ... Valcke, S. (2021). Tracking Changes in Climate Sensitivity in CNRM
809 Climate Models. *Journal of Advances in Modeling Earth Systems*, 13(6), 1–19.
810 doi: 10.1029/2020MS002190
- 811 Shamekh, S., Muller, C., Duvel, J. P., & D’Andrea, F. (2020a). How do ocean warm
812 anomalies favor the aggregation of deep convective clouds? *Journal of the At-*
813 *mospheric Sciences*, 77(11), 3733–3745. doi: 10.1175/JAS-D-18-0369.1
- 814 Shamekh, S., Muller, C., Duvel, J. P., & D’Andrea, F. (2020b). Self-Aggregation of
815 Convective Clouds With Interactive Sea Surface Temperature. *Journal of Ad-*
816 *vances in Modeling Earth Systems*, 12(11). doi: 10.1029/2020MS002164
- 817 Stein, T. H., Holloway, C. E., Tobin, I., & Bony, S. (2017). Observed relation-
818 ships between cloud vertical structure and convective aggregation over tropical
819 ocean. *Journal of Climate*, 30(6), 2187–2207. doi: 10.1175/JCLI-D-16-0125.1
- 820 Tobin, I., Bony, S., Holloway, C. E., Grandpeix, J.-Y., Sèze, G., Coppin, D., ...
821 Roca, R. (2013). Does convective aggregation need to be represented in cumu-
822 lus parameterizations? *Journal of Advances in Modeling Earth Systems*, 5(4),
823 692–703. doi: 10.1002/jame.20047
- 824 Tobin, I., Bony, S., & Roca, R. (2012). Observational evidence for relation-

- 825 ships between the degree of aggregation of deep convection, water vapor,
 826 surface fluxes, and radiation. *Journal of Climate*, 25(20), 6885–6904. doi:
 827 10.1175/JCLI-D-11-00258.1
- 828 Tompkins, A. M., & Craig, G. C. (1998). Radiative-convective equilibrium in a
 829 three-dimensional cloud-ensemble model. *Quarterly Journal of the Royal Mete-*
 830 *orological Society*, 2073–2097. doi: 10.1002/qj.49712455013
- 831 Tompkins, A. M., & Semie, A. G. (2017). Organization of tropical convection in
 832 low vertical wind shears: Role of updraft entrainment. *Journal of Advances in*
 833 *Modeling Earth Systems*, 9, 1046–1068. doi: 10.1002/2016MS000802
- 834 Voldoire, A., Saint-Martin, D., S en esi, S., Decharme, B., Alias, A., Chevallier, M.,
 835 ... Waldman, R. (2019). Evaluation of CMIP6 DECK Experiments With
 836 CNRM-CM6-1. *Journal of Advances in Modeling Earth Systems*, 11(7), 2177–
 837 2213. doi: 10.1029/2019MS001683
- 838 Wing, A. A. (2019). Self-Aggregation of Deep Convection and its Implications for
 839 Climate. *Current Climate Change Reports*, 5(1), 11–13. doi: 10.1007/s40641
 840 -019-00120-3
- 841 Wing, A. A., & Cronin, T. W. (2016). Self-aggregation of convection in long channel
 842 geometry. *Quarterly Journal of the Royal Meteorological Society*, 142(694), 1–
 843 15. doi: 10.1002/qj.2628
- 844 Wing, A. A., Emanuel, K., Holloway, C. E., & Muller, C. (2017). Convective Self-
 845 Aggregation in Numerical Simulations: A Review. *Surveys in Geophysics*,
 846 38(6), 1173–1197. doi: 10.1007/s10712-017-9408-4
- 847 Wing, A. A., & Emanuel, K. A. (2014). Physical mechanisms controlling
 848 self-aggregation of convection in idealized numerical modeling simula-
 849 tions. *Journal of Advances in Modeling Earth Systemsd*, 6, 59–74. doi:
 850 10.1002/2013MS000269
- 851 Wing, A. A., Reed, K. A., Satoh, M., Stevens, B., Bony, S., & Ohno, T. (2018).
 852 Radiative-convective equilibrium model intercomparison project. *Geoscientific*
 853 *Model Development*, 11(2), 793–813. doi: 10.5194/gmd-11-793-2018
- 854 Wing, A. A., Stauffer, C. L., Becker, T., Reed, K. A., Ahn, M. S., Arnold, N. P., ...
 855 Zhao, M. (2020). Clouds and Convective Self-Aggregation in a Multimodel En-
 856 semble of Radiative-Convective Equilibrium Simulations. *Journal of Advances*
 857 *in Modeling Earth Systems*, 12(9), 1–38. doi: 10.1029/2020MS002138

858 Yang, D. (2018). Boundary Layer Diabatic Processes, the Virtual Effect, and Con-
859 vective Self-Aggregation. *Journal of Advances in Modeling Earth Systems*,
860 10(9), 2163–2176. doi: 10.1029/2017MS001261

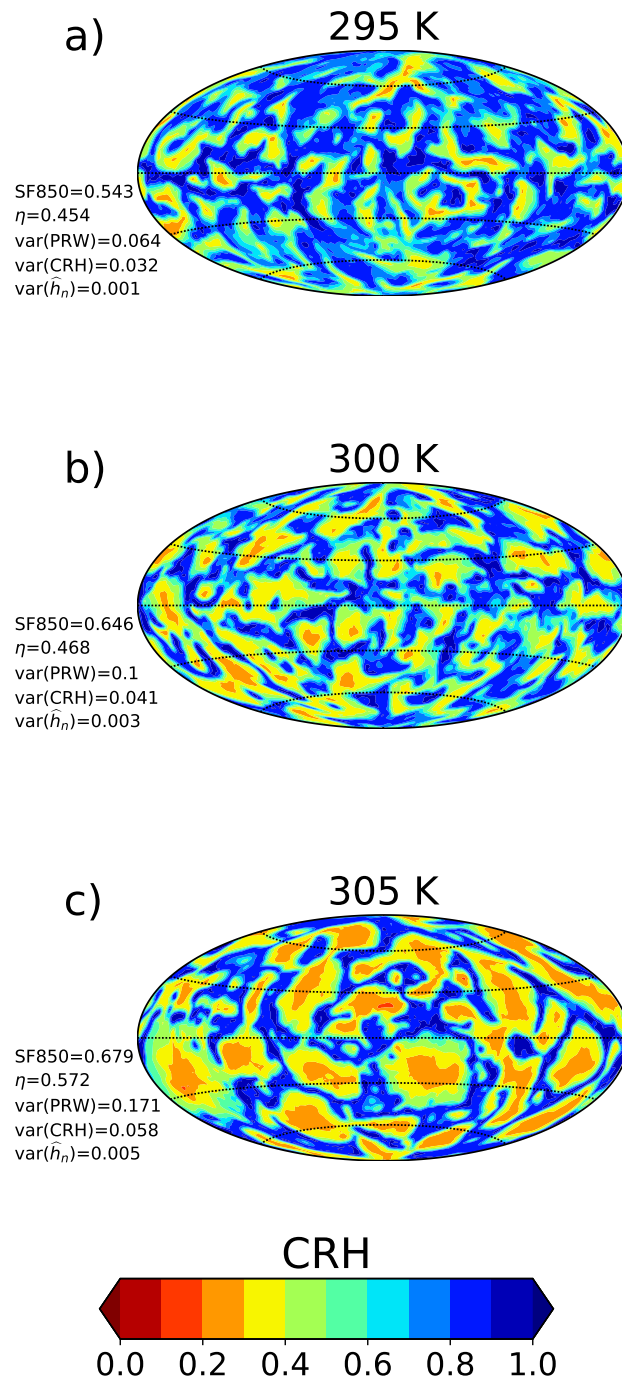


Figure 1. Snapshots of column relative humidity at day 240 of the CNRM-CM6-1 RCE simulations at (a) 295 K, (b) 300 K and (c) 305 K. Different aggregation indices used to characterize convective aggregation are noted in the bottom left corner of each panel (SF850: subsiding fraction considering the pressure vertical velocity at 850 hPa; η : shallow circulation efficiency parameter (see text for detail); $\text{var}(\text{PRW})$: spatial variance of precipitable water; $\text{var}(\text{CRH})$: spatial variance of CRH; $\text{var}(\hat{h}_n)$: spatial variance of normalized MSE).

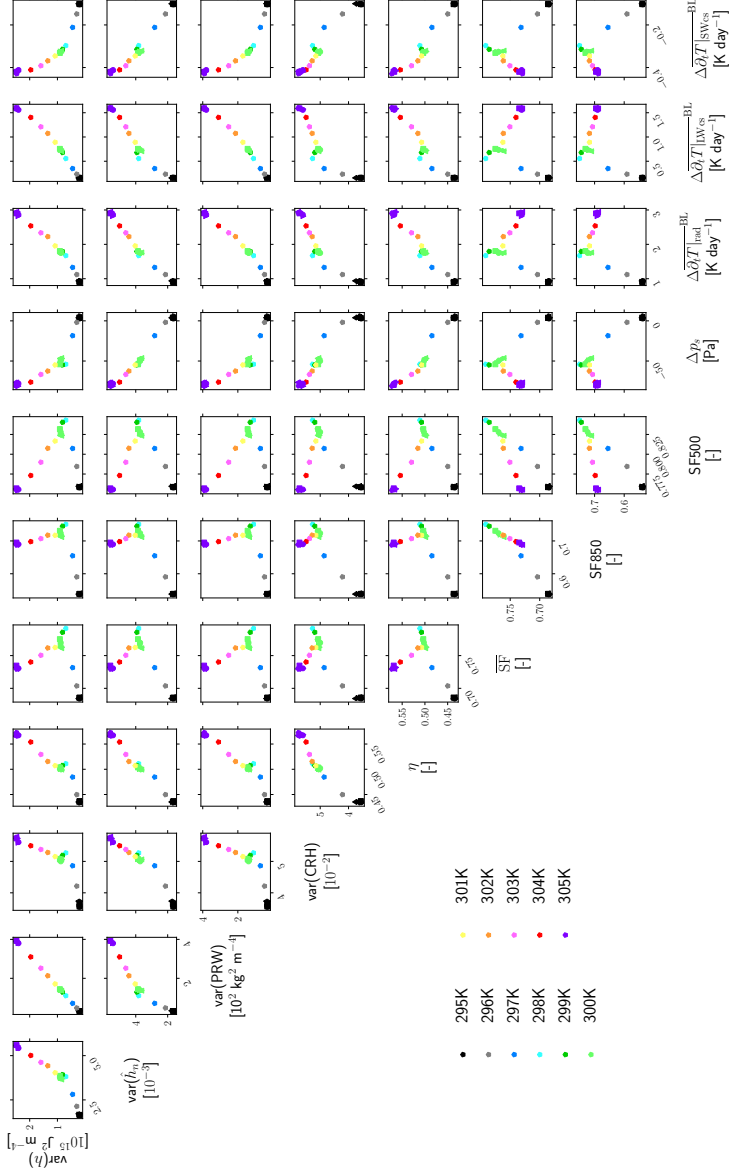


Figure 2. Matrix of the relationships between various indices computed for each SST equilibrium: $\text{var}(\hat{h})$ (in $10^{15} \text{ J}^2 \text{ m}^{-4}$), $\text{var}(\hat{h}_n)$ (in 10^{-3}), $\text{var}(\text{PRW})$ (in 10^2 m^{-4}), $\text{var}(\text{CRH})$ (in 10^{-2}), η , $\overline{\text{SF}}$, SF850 and SF500 (see text for their definition). Each panel shows the relationship between two indices as indicated along the matrix diagonal for all SSTs (colors) and for all members of each 295-K, 300-K and 305-K ensemble (same color within each ensemble). The last four columns illustrate the relationships between these indices and the differences between moist and dry regions (Δp_s in Pa) for the surface pressure (Δp_s in Pa) and the boundary-layer net, LW clear-sky and SW clear-sky radiative temperature tendencies ($\overline{\Delta \partial_t T}|_{\text{rad}}^{\text{BL}}$, $\overline{\Delta \partial_t T}|_{\text{LWcs}}^{\text{BL}}$, and $\overline{\Delta \partial_t T}|_{\text{SWcs}}^{\text{BL}}$, respectively, in K day^{-1}). Both regions are defined according to CRH $_c$. The boundary layer values are calculated as the weighted average between 1000 hPa and 925 hPa. Each dot corresponds to the time average over the last year of the corresponding 3-year simulation.

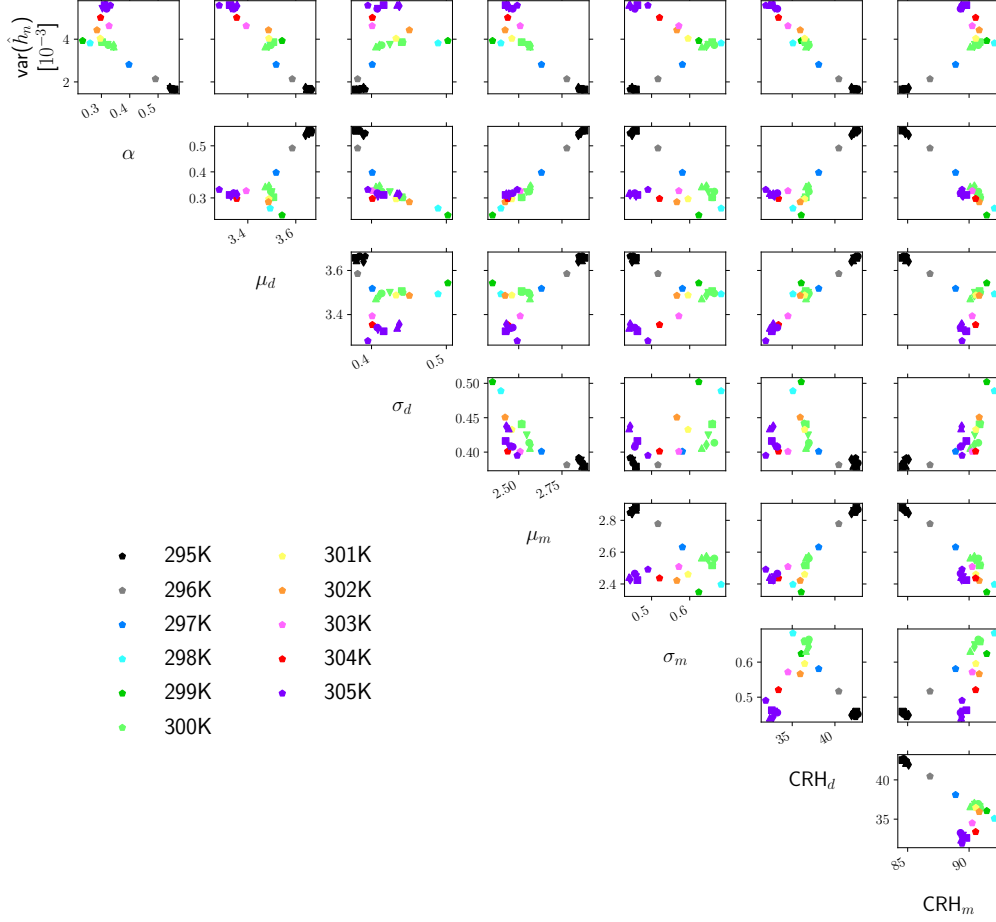


Figure 3. Matrix of the relationships across SSTs between the \hat{h}_n variance (in 10^{-3}) and several parameters describing the CRH distribution at equilibrium: α , μ_d , σ_d , μ_m , σ_m , CRH_d and CRH_m (see Section 2.4 for their definition). Each panel shows the relationship between two indices as indicated along the matrix diagonal for all SSTs (colors) and for all members of each 295-K, 300-K and 305-K ensemble (same color within each ensemble). Each dot corresponds to the time average over the last year of the corresponding 3-year simulation.

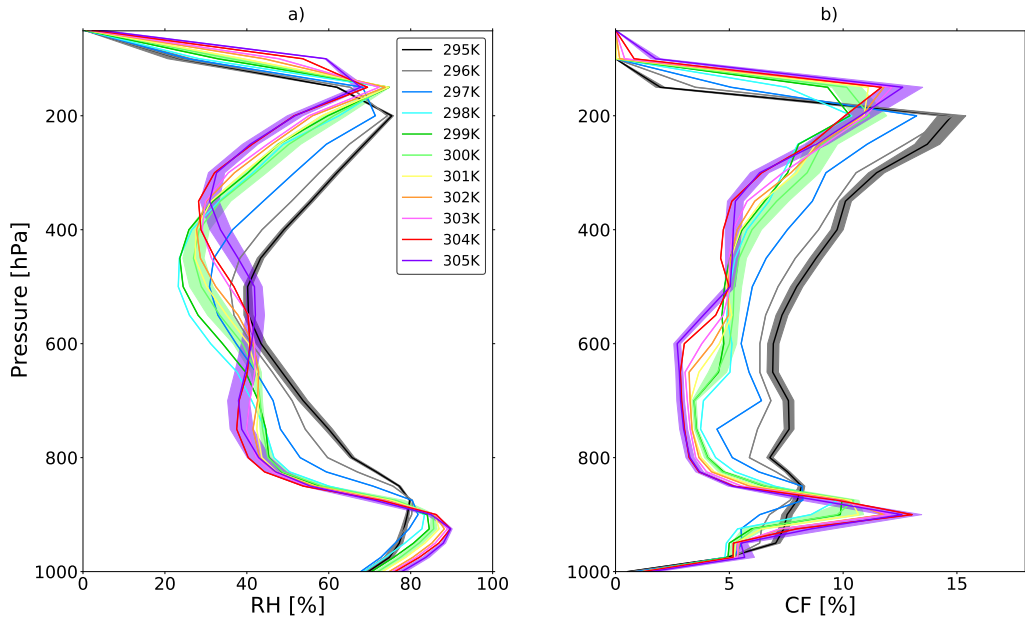


Figure 4. Global mean profile of (a) relative humidity (RH, in %) and (b) cloud fraction (CF, in %) for all SSTs (colored lines). The shading indicates the 3-standard-deviation envelope of the 295-K, 300-K and 305-K ensembles. The time average is performed over the last year of each 3-year simulation.

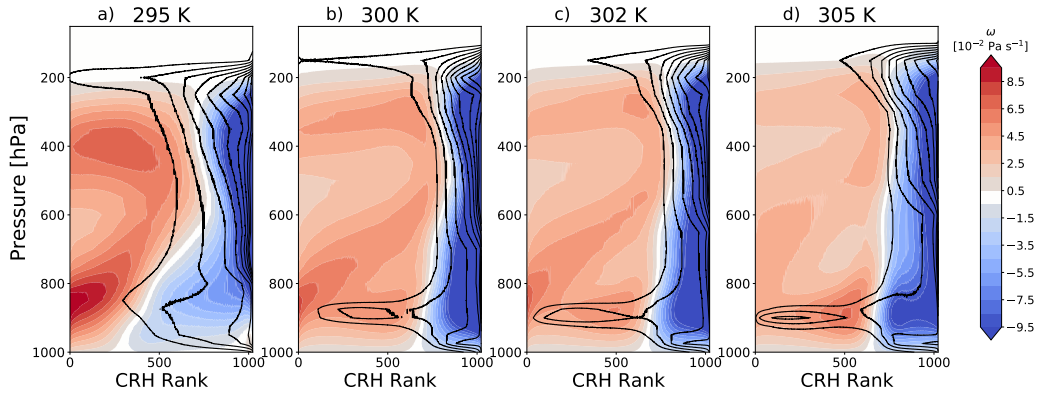


Figure 5. Pressure vertical velocity (colors, in $10^{-2} \text{ Pa s}^{-1}$) and cloud fraction (contours, every 5%) ranked by the daily column relative humidity CRH from dry on the left to moist on the right, for the (a) 295-K, (b) 300-K, (c) 302-K and (d) 305-K simulations. For the sake of clarity, each rank of daily CRH corresponds to the average 32 model columns. Each panel is then an average over the last year of each 3-year simulation.

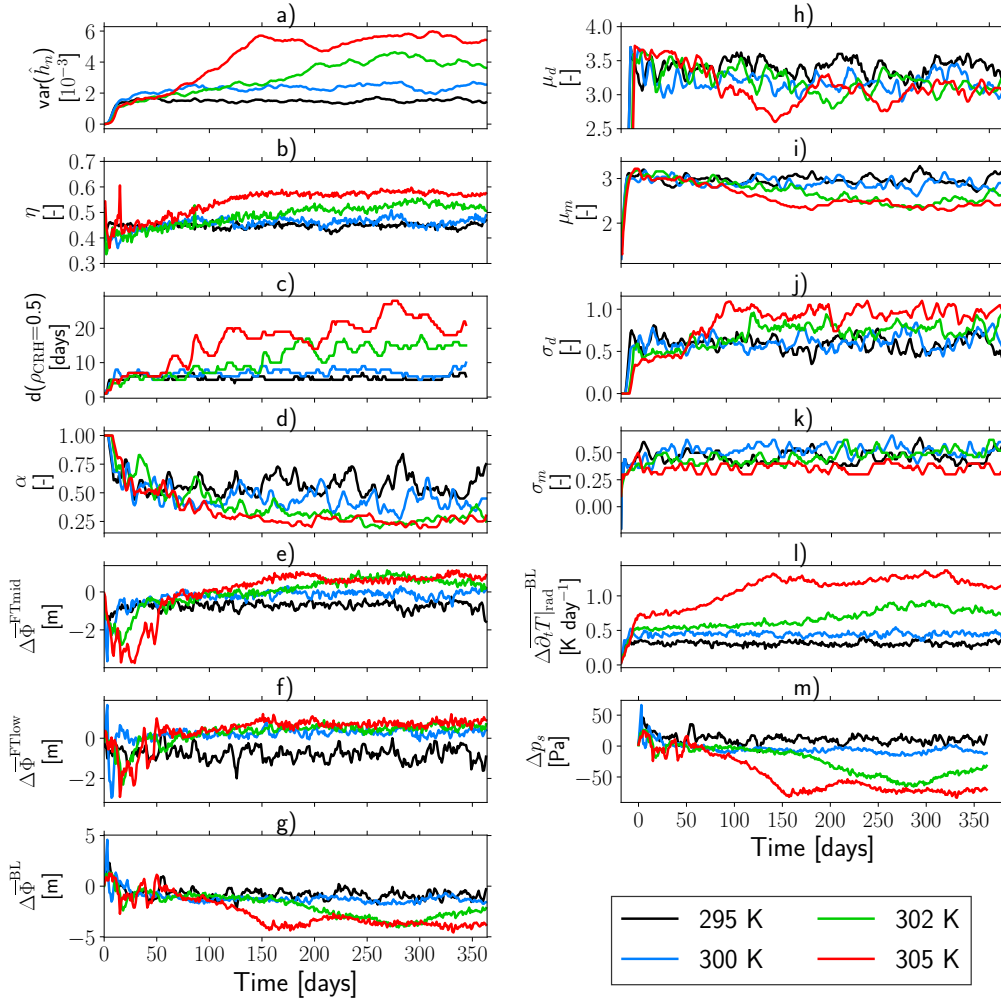


Figure 6. (a) Time evolution of the \hat{h}_n variance over the first year of the 295 K (black), 300 K (blue), 302 K (green) and 305 K (red) simulations. (b-m) Same as (a) but for the shallow circulation efficiency η , the maximum lead time (in days) for which the CRH autocorrelation remains above 0.5 ($d(\rho_{\text{CRH}}=0.5)$), the fraction α of the moist distribution in the CRH full distribution, the geopotential height difference (in m) between moist and dry regions (Δ symbol) integrated over the mid free troposphere (600-400 hPa, $\overline{\Delta\Phi}^{\text{FTmid}}$), the lower free troposphere (850-700 hPa, $\overline{\Delta\Phi}^{\text{FTlow}}$) and the boundary layer (1000-900 hPa, $\overline{\Delta\Phi}^{\text{BL}}$), the CRH distribution parameters (see section 2.4 for details), the radiative temperature tendency difference between moist and dry regions integrated over the boundary layer (1000-900 hPa, $\overline{\Delta\partial_t T}_{\text{rad}}^{\text{BL}}$ in K day $^{-1}$) and the surface pressure difference between moist and dry regions (Δp_s in Pa), respectively. Both dry and moist regions are separated according to CRH_c .

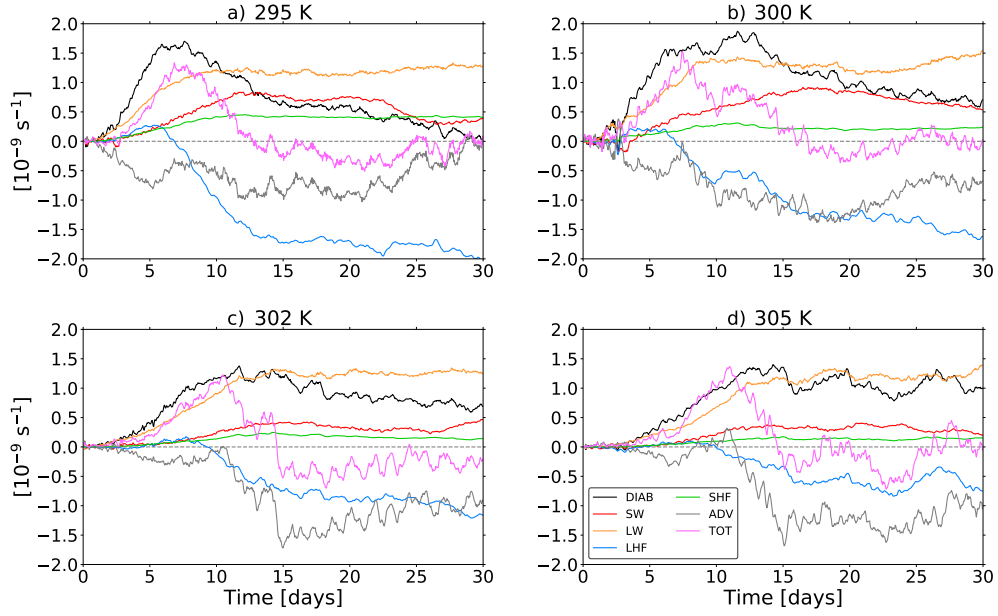


Figure 7. Time evolution of the diabatic (DIAB=SW + LW + LHF + SHF, black), short-wave radiation (SW, red), longwave radiation (LW, orange), latent heat flux (LHF, blue), sensible heat flux (SHF, green), advection (ADV, grey) and total (TOT, purple) feedbacks on the \hat{h}_n variance (in 10^{-9} s^{-1}) for the first 30 days of the (a) 295-K, (b) 300-K, (c) 302-K, and (d) 305-K simulations. The advection feedback is calculated using hourly wind and FMSE model outputs (results are similar when using the more usual residual approach based on Equation 3).

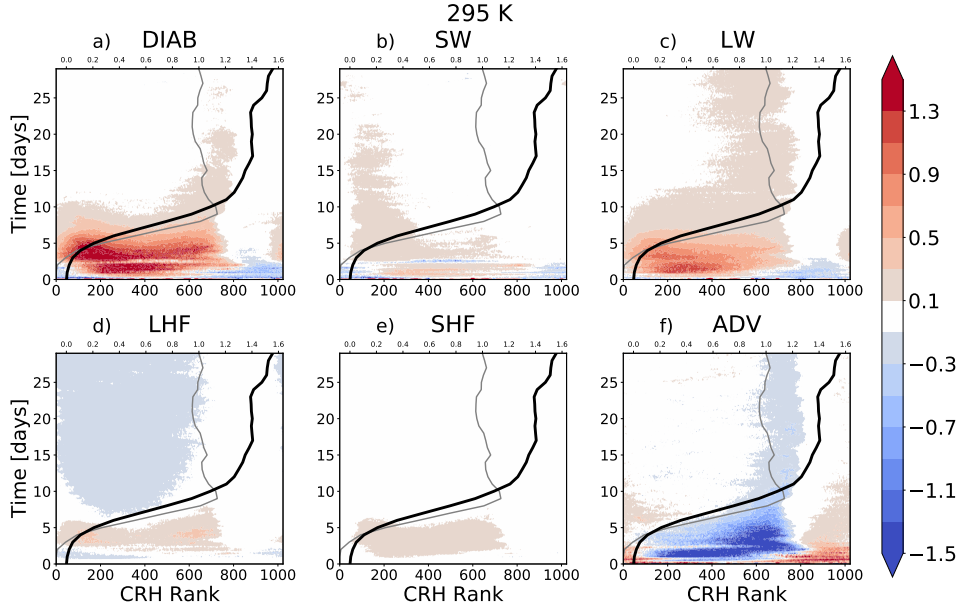


Figure 8. Time evolution of the (a) diabatic (DIAB = SW + LW + LHF + SHF) (b) short-wave radiation (SW), (c) longwave radiation (LW), (d) latent heat flux (LHF), (e) sensible heat flux (SHF), and (f) advection (ADV) feedbacks on the \hat{h}_n variance (in day^{-1}) for the first 30 days of the 295-K simulation and ranked according to the column relative humidity CRH. Feedbacks are normalized at each time step by the corresponding spatial variance of \hat{h}_n . The advection feedback is calculated using hourly model outputs. The black and grey solid lines indicate the time evolution of the \hat{h}_n variance (in 10^{-3} , see upper x -axis for its scale) and the CRH rank corresponding to CRH_c , respectively.

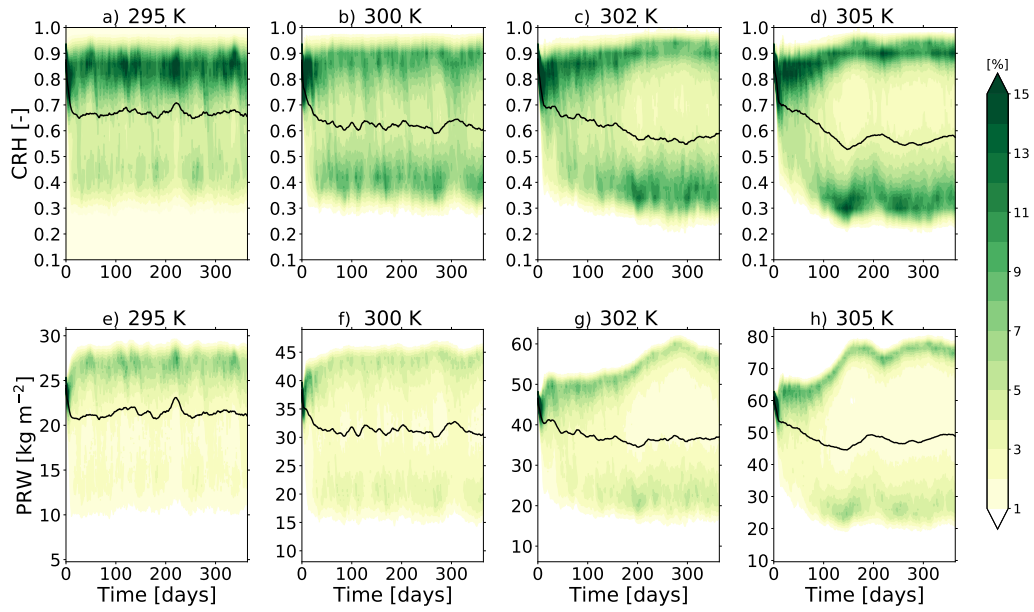


Figure 9. Time evolution of the CRH distribution (in %) for the (a) 295-K, (b) 300-K, (c) 302-K and (d) 305-K simulations. The black line shows the global mean. (e-h) Same as (a-d) for precipitable water.

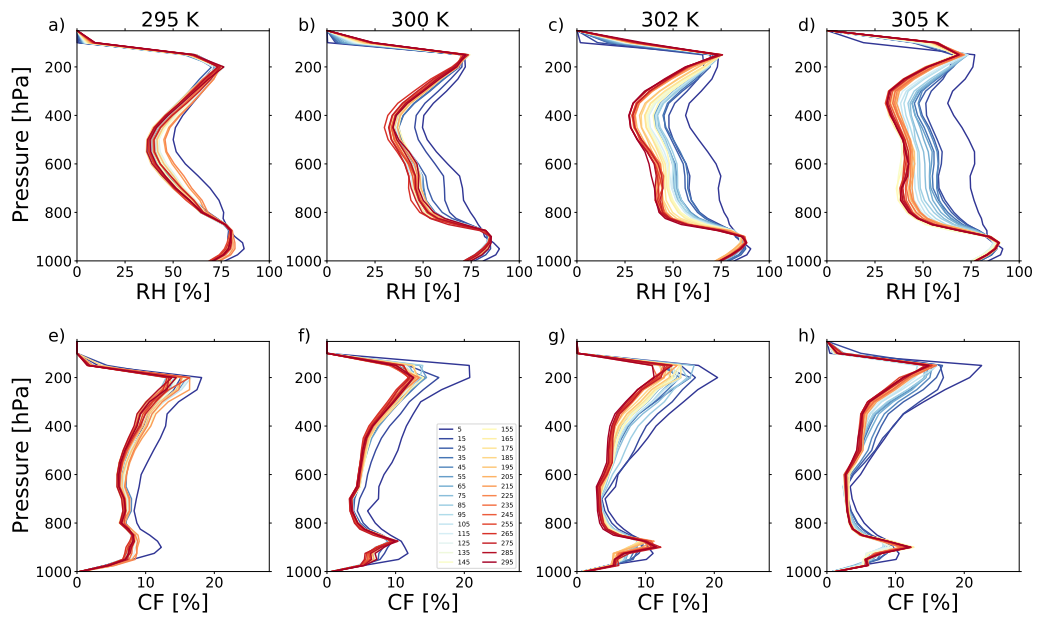


Figure 10. Global mean profile of (a-d) relative humidity (RH, in %) and (e-h) cloud fraction (CF, in %) for the 295-K, 300-K, 302-K and 305-K simulations, respectively. The colors from dark blue to dark red indicate increasing days at which the profile is plotted (from day 5 to day 295, one profile every 5 days).

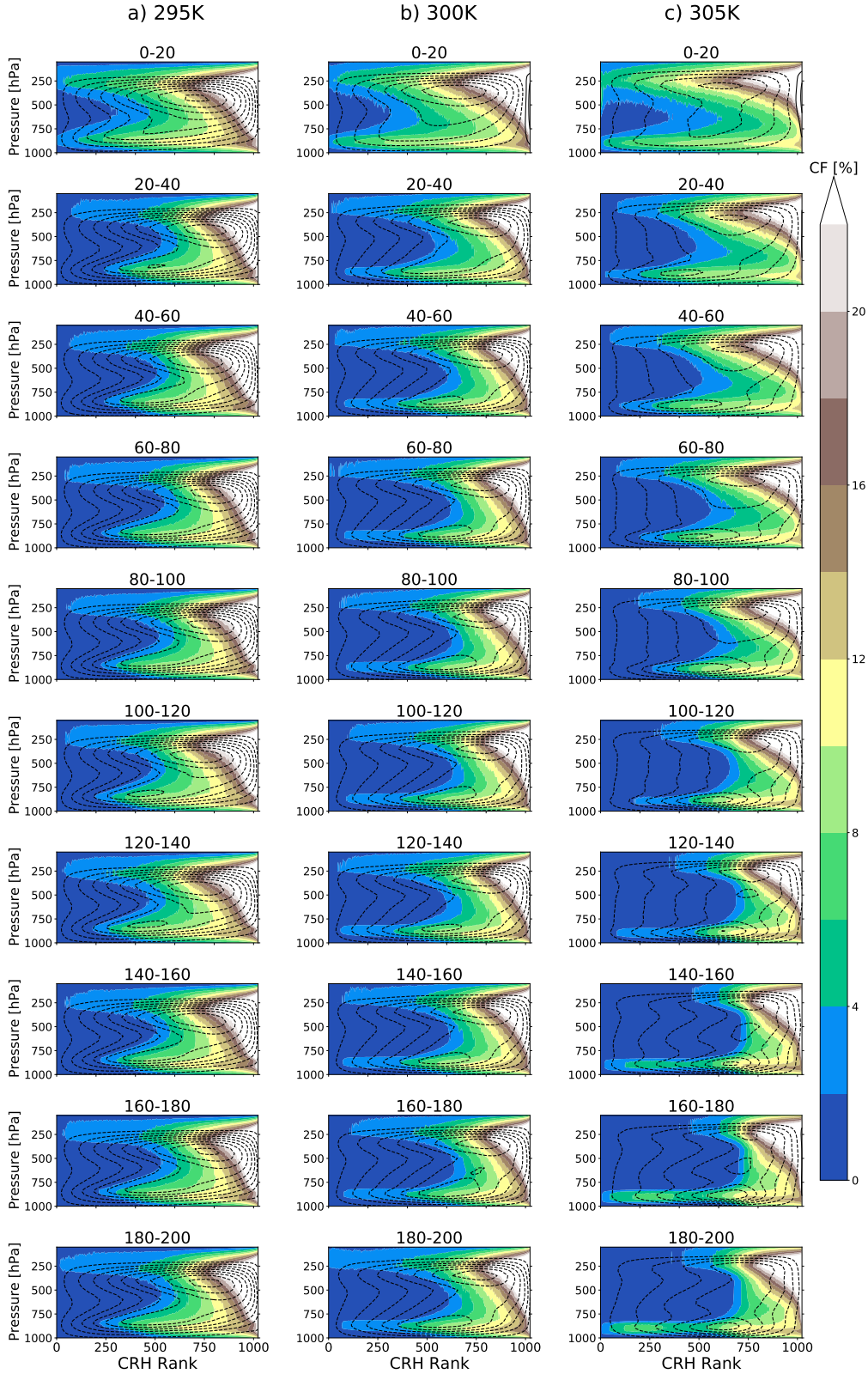


Figure 11. Cloud fraction (colors, in %) and streamfunction (contours, one every $0.5 \text{ kg m}^{-2} \text{ s}^{-1}$) averaged over 20 consecutive days between days 0 and 200 for the (a) 295-K, (b) 300-K and (c) 305-K simulations. Dashed contours indicate counter-clockwise rotation. For the sake of clarity, each rank of daily CRH corresponds to the average of 32 model columns. Each panel is then the average of 20 diagrams corresponding to the targeted 20 days. The streamfunction is computed from similar average diagrams based on the vertical velocity (see appendix A for details)

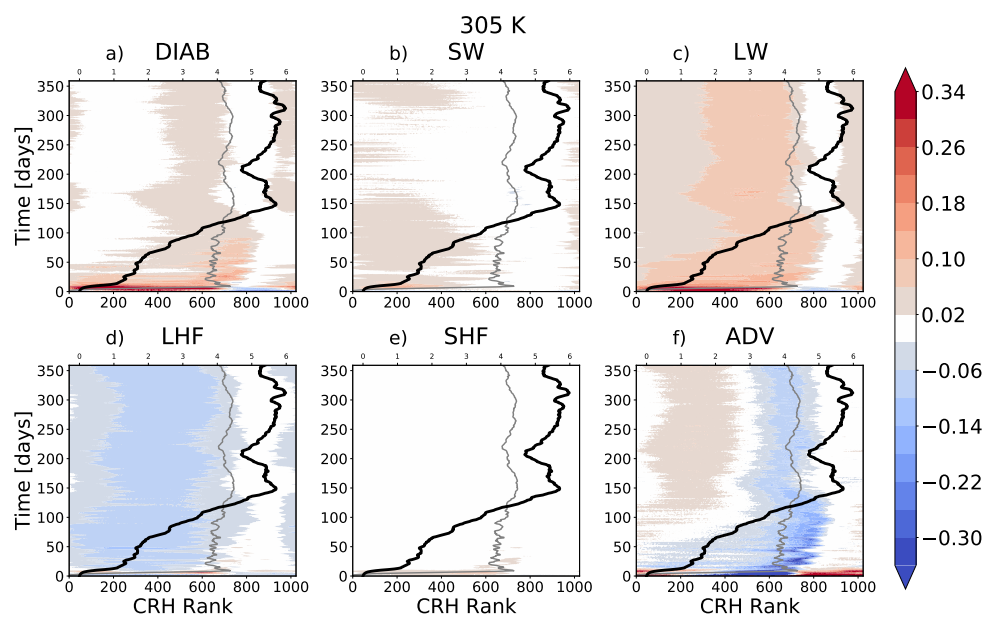


Figure 12. Same as Figure 8 but for the first 360 days of the 305-K simulation.

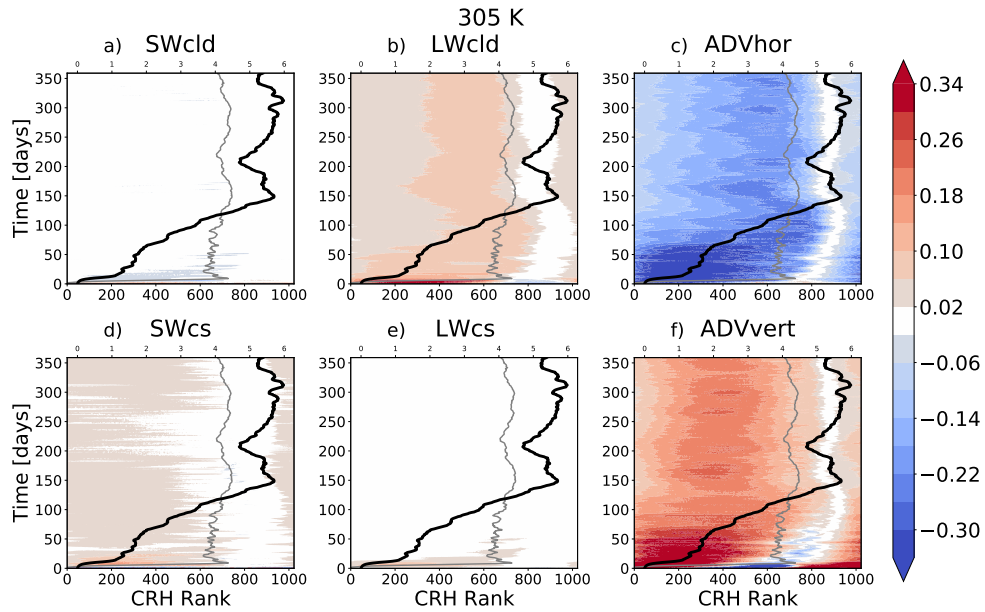


Figure 13. Time evolution of the (a) cloudy-sky shortwave radiation (SWcld), (b) cloudy-sky longwave radiation (LWcld), (c) horizontal advection (ADVhor), (d) clear-sky shortwave radiation (SWcs) (e) clear-sky longwave radiation (LWcs) and (f) vertical advection (ADVvert) feedbacks on the normalized FMSE variance (in day^{-1}) for the first 360 days of the 305-K simulation and ranked according to CRH. Feedbacks are normalized at each time step by the corresponding spatial variance of \hat{h}_n . The horizontal and vertical advection feedbacks are calculated using hourly model outputs. The black and grey lines indicate the time evolution of the \hat{h}_n variance (see upper x -axis for its scale) and the CRH rank corresponding to CRH_c , respectively.

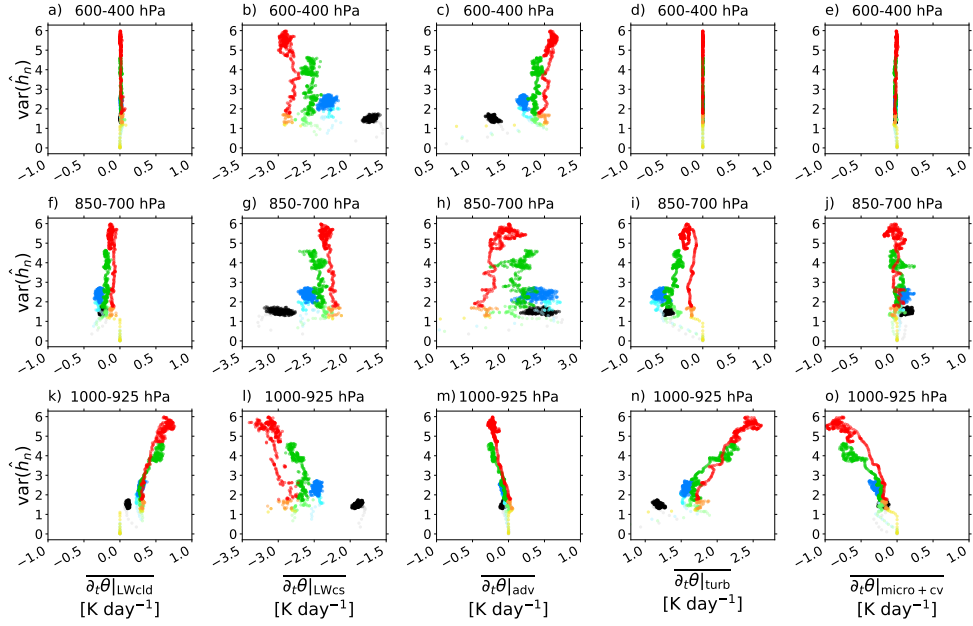


Figure 14. Daily \hat{h}_n spatial variance (in 10^{-3}) evolution over the first year of the 295-K (black), 300-K (blue), 302-K (green) and 305-K (red) simulations as a function of the (a) cloudy-sky longwave radiation, (b) clear-sky longwave radiation, (c) advection, and (d) turbulence potential temperature tendencies ($\overline{\partial_t \theta}|_{\text{LWcld}}$, $\overline{\partial_t \theta}|_{\text{LWcs}}$, $\overline{\partial_t \theta}|_{\text{adv}}$ and $\overline{\partial_t \theta}|_{\text{turb}}$, respectively) and (e) the sum of the convection and large-scale condensation-evaporation ($\overline{\partial_t \theta}|_{\text{micro+cv}}$) temperature tendencies (in K day^{-1}). All terms are averaged over the 600-400-hPa layer and tendencies are daily accumulated. Light colors indicate the first 50 days of each simulation. (f-j) and (k-o) same as (a-e) but for the 850-700-hPa and 1000-925-hPa atmospheric layers, respectively.

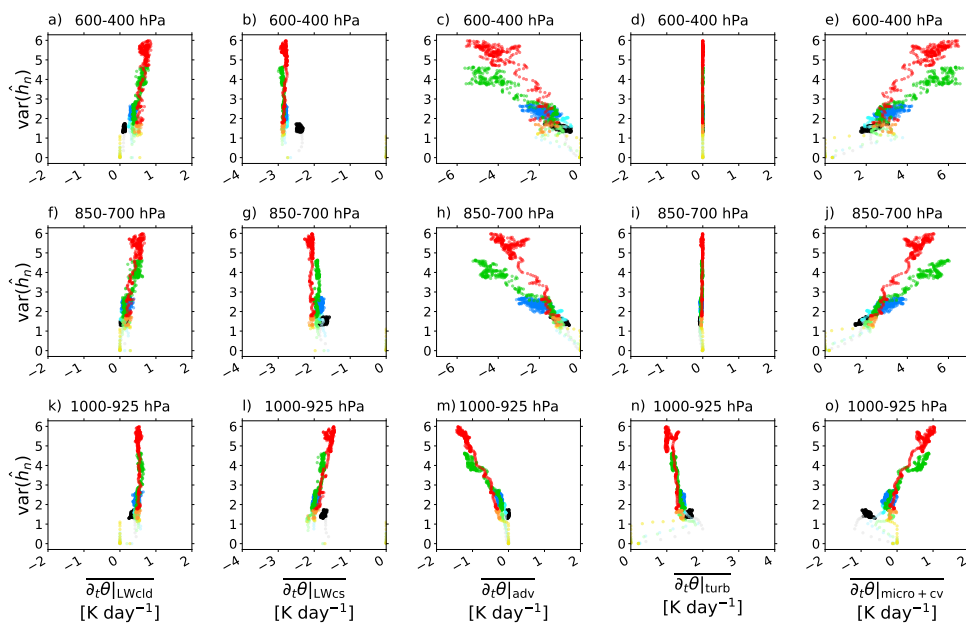


Figure 15. Same as Figure 14 for moist regions.